

A Scaler-Based Data Acquisition System for Measuring Parity Violation Asymmetry in Deep Inelastic Scattering

by

Kai Pan

B.S., University of Science and Technology of China (2008)

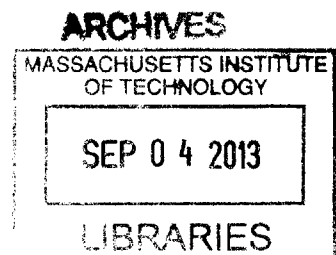
Submitted to the Department of Physics
in partial fulfillment of the requirements for the degree of
Master of Science in Physics

at the

MASSACHUSETTS INSTITUTE OF TECHNOLOGY

February 2013

© 2013 Massachusetts Institute of Technology. All rights reserved.



Author
.....

Department of Physics
February 1, 2013

Certified by...
.....

William Bertozzi
Professor of Physics
Thesis Supervisor

Certified by...
.....

Shalev Gilad
Principal Research Scientist
Thesis Co-Supervisor

Accepted by
.....

John Belcher
Associate Department Head

A Scaler-Based Data Acquisition System for Measuring Parity Violation Asymmetry in Deep Inelastic Scattering

by

Kai Pan

Submitted to the Department of Physics
on February 1, 2013, in partial fulfillment of the
requirements for the degree of
Master of Science in Physics

Abstract

An experiment that measured the parity violating (PV) asymmetry A_d in e^-H deep inelastic scattering (DIS) at $Q^2 \approx 1.10$ and 1.90 (GeV/c^2)² and $x_B \approx 0.3$ was completed in experimental Hall A at the Thomas Jefferson National Accelerator Facility. The asymmetry can be used to extract the neutral weak coupling combination $(2C_{2u} - C_{2d})$, providing a factor of five to six improvement over the current world data. To achieve this precision, asymmetries of the 10^{-4} level needed to be measured at event rates up to 500 kHz with high electron detection efficiency and high pion background rejection capability. A specialized scaler-based counting data acquisition system (DAQ) with hardware-based particle identification was successfully implemented. The overall pion contamination in the electron sample was controlled to approximately 2×10^{-4} or lower with an electron efficiency above 91% throughout the experiment. The DAQ deadtime contributed an approximately 0.2% uncertainty to the final asymmetries. The statistical quality of the asymmetry measurement agreed with the Gaussian distribution to over five orders of magnitudes and the experimental goal of 3-4% statistical uncertainty was achieved. The results presented here demonstrate that this type of scaler-based DAQ is able to perform accurate measurements of small asymmetries at the 1ppm level. The design of the DAQ system is presented including the analysis of PID performance, deadtime effect and the capability of measuring small asymmetries.

Thesis Supervisor: William Bertozzi
Title: Professor of Physics

Thesis Co-Supervisor: Shalev Gilad
Title: Principal Research Scientist

Acknowledgments

This thesis marks the end of a challenging but fruitful journey. The experience in the past four years in every aspect of my life is profoundly memorable, and my heart is filled with nothing but gratitude.

First and foremost, I would like to thank my advisors Prof. William Bertozzi and Dr. Shalev Gilad, for leading me through the difficult period of my life with their constant trust, understanding and encouragement, both academically and personally. Their inspirational advice is beyond measure, and it is my great honor to learn dedication, perseverance and sacrifice from them.

I also want to thank the E08-011 collaboration for this successful experiment and the opportunity for my thesis research. I would like to thank the co-spokespersons, Xiaochao Zheng, Paul E. Reimer and Bob Michaels, for their leadership on this experiment, guidance on my work and advices on my career choices. Special thanks goes to Prof. Xiaochao Zheng for being my research advisor at JLab and for her thorough understanding of the subject of my thesis experiment; also for her friendship that helped me through the difficult time in both academia and personal life. Not only her excellence in nuclear physics research, but also her capability to maintain good family life was very impressive. I thank the postdocs and my fellow graduate students of this experiment, Ramesh Subedi, Zhaozhi Wen, Diancheng Wang and Xiaoyan Deng, for their excellent work and kind help on my research. I wish everyone success and happiness.

I want to thank other members of the MIT Nuclear Interaction Group, Vincent Sulkosky, Qiang Yi, Xiaohui Zhan, Jin Huang, Navaphon Muangma and Aidan Kelleher. Our postdoc, Vincent Sulkosky reviewed this thesis and offered numerous valuable comments, and I am sincerely grateful for his help. I would also like to thank Dr. Xin Qian in Caltech for his help not only in my research but also in my personal life. Both Jin Huang and Xin Qian are acting more like my senior brothers rather than normal friends. I couldn't achieve today's result without their consistent help and encouragement.

I am grateful for the brotherhood and friendship with many people on this campus and in JLab. Sharing life with them has been invaluable. I wish the best of luck to all of them.

Finally, I deeply appreciate the love and support of my family. I can not think of words to thank them enough for all they have done for me.

Contents

1	Introduction	15
1.1	The Running of $\sin^2 \theta_w$	15
1.2	Weak Neutral Current Couplings at Low Q^2	17
1.3	Parity Violation in Deep Inelastic Scattering and the Standard Model	18
1.4	Experiment Overview	21
2	Apparatus	23
2.1	Overview	23
2.2	Polarized Electron Beam	24
2.3	Beam Monitoring	26
2.3.1	Beam Current Monitor (BCM)	26
2.3.2	Beam Position Monitor (BPM)	27
2.4	Target	28
2.5	Hall A Spectrometers	29
3	A New Scaler-based Data Acquisition System (DAQ)	31
3.1	Motivation	31
3.2	DAQ Design	32
4	Data Analysis	39
4.1	Overview of Data Taking	39
4.2	Data selection and Cuts	40
4.3	Beam Corrections and Systematic Fluctuations	42

4.4	Beam Polarimetry	44
4.4.1	Møller Polarimeter	44
4.4.2	Compton Polarimeter	46
4.4.3	Beam Polarization Results	46
4.5	Beam Position Calibration	49
4.6	Calibration of the HRS Optics	49
4.6.1	VDC Timing Calibration	51
4.6.2	Optics Matrix Calibration and Systematic Uncertainties	52
4.6.3	Optics Calibration Results	55
4.6.4	Q^2 Uncertainties	57
4.7	DAQ PID Performance	57
4.8	DAQ Deadtime	67
4.8.1	Deadtime Overview	67
4.8.2	Trigger Simulation	68
4.8.3	Group Deadtime Measurement	69
4.8.4	VETO Deadtime Measurement	72
4.8.5	“OR” Deadtime Measurement	72
4.8.6	Total Deadtime Evaluation	72
4.9	Asymmetry Measurement	72
5	Summary and Proposed Future Work	77
	Bibliography	78

List of Figures

1-1	Theoretical curve of the running of $\sin^2 \theta_w$ and existing measurements from Cs APV, Fermilab NuTeV, SLAC E158 Møller. Also shown is expected uncertainty of the JLab QWeak experiment.	16
1-2	Tree-level Feynman diagrams for electron scattering.	19
2-1	Floor plan of the PVDIS experiment in Hall A at Jefferson Lab. Beam enters from the left and scatters from a LD ₂ target. The scattered electrons are detected in the two HRS (High Resolution Spectrometer) detector stacks. Reproduced from [1].	25
2-2	Locations of the BPMs and BCMs, along with the beam modulation (BM) coils used during E08-011. BPM4b and BPM4a were located 1.3 and 7.5m upstream of the target, respectively. BCM1 and BCM2 were separated by 3m. Reproduced from [2].	26
2-3	Rastered beam spot distribution at the target.	29
2-4	Schematic of a Hall A High Resolution Spectrometer and the detector package. Reproduced from [3].	30
3-1	Grouping scheme (side-view) for the double-layer lead-glass detectors in the Left and the Right HRS. Index number of lead-glass blocks in both preshower and shower detector of Left and Right HRS is shown. Scattered particles enter the detector from the left. The colored vertical bars represent the range of each group.	34

3-2 Electronics diagram for the Right HRS DAQ used by the E08-011 experiment. The Sum8's, discriminators and logic modules for two groups are shown, as well as the location of tagger signal inputs, setup of the VETO circuit using scintillator (SC) and gas Cherenkov (GC) signals, the logic units for combining triggers from all eight groups into final triggers, the counting scalers, and the monitoring fastbus TDCs. Electronics for the Left HRS was similar except for the grouping scheme.	36
4-1 Polarization history from the Møller polarimeter measurements. The error bars include systematic uncertainties.	47
4-2 Polarization history from the Compton polarimeter measurements (round points), together with Møller measurements (square points) during the same time. The error bars for Compton are statistical only, while Møller includes systematic uncertainties.	48
4-3 Beam position reconstruction before (top) and after (bottom) BPM calibration. The blue lines are the beam positions determined by the BPMs, and the red lines are the beam positions determined by the raster current.	50
4-4 A drift-time Spectrum of a VDC plane.	51
4-5 Drift-time spectrum of all wires in VDC U1 plane before (left) and after (right) T_0 timing correction.	52
4-6 Target coordinates of the scattered event and the coordinates of the sieve plane (topview). ϕ_{tg} is the in-plane angle with regard to. the spectrometer central ray and θ_{tg} is the out-of- plane angle. The y-sieve axis is pointing to the left of the spectrometer entrance and the x-sieve axis points vertically down. Reproduced from [1].	53
4-7 Vertex reconstruction of left kinematics 1. The numbers shown in the plot are the difference between the reconstructed target position and target survey position.	56

4-8	Sieve reconstruction of left kinematics 1. Grid lines represent the sieve-hole survey position.	56
4-9	An ADC signal of the right HRS gas Cherenkov detector without a cut (black), after lead glass detector's electron cut (red) and pion cut (blue). The vertical green line shows a cut $ADC > 1500$ for selecting electrons, and the vertical magenta line shows a cut $ADC < 30$ for selecting pions.	59
4-10	Two-dimensional distribution of signals strength in Preshower and Shower lead glass detector, after the gas Cherenkov ADC electron cut (red) and the pion cut (blue). The green box shows a cut for selecting clean electron sample, and the magenta box shows a cut for selecting clean pion sample.	60
4-11	fbTDC signal of electron global counter.	61
4-12	Preshower vs. Shower ADC spectrum (sum of 8 blocks each) for group 2 of the Left HRS without a fbTDC cut (left) and with cut on the group 2 electron wide trigger fbTDC signal (right). The events near the vertical axis, around ADC channels (200,1000), are electrons that deposited energy in overlapping blocks between group 2 and group 1 (or group 3) and are recorded by the other group.	61
4-13	Electron detection efficiency (left) and pion rejection factor (right) vs. vertical (dispersive) hit position of particles in the preshower detector for the narrow electron triggers in the Left HRS. For electron efficiencies, the total efficiency is shown by the red curve, while blue shaded area indicates events that are recorded by the two adjacent groups. The error bars are statistical only. PID performance for the wide path and the Right HRS are similar.	62
4-14	Gas Cherenkov ADC data (sum of 10 PMTs) for the Left HRS with a fbTDC cut on the Cherenkov discriminator output (red) and without (black).	63

4-15 Calibration of time constant τ for Preshower (left) and Shower (right) of the Right HRS. The FADC snapshot (black) is compared with the fit $S(t) = Ate^{-t/\tau}$ (red).	69
4-16 Top: A part of the group electron trigger. The numbers correspond to: 1 - Shower sum of the group; 2 - Total shower sum of the group; 3 - Total shower discriminator output (high threshold), narrow path; 4 - Preshower discriminator output (medium threshold), narrow path; 5 - group electron trigger, narrow path; 6 - Total shower discriminator output, wide path; 7 - Preshower discriminator output, wide path; 8 - group electron trigger, wide path. Bottom: Signals 1-8 as simulated by HATS. Note that the second physical event is recorded by the narrow path group trigger (5) but not the wide path (8) due to deadtime loss.	70
4-17 schematic diagram of the tagger setup and signal timing sequence.	71
4-18 Overall statistical quality of the data after the dithering correction. From top to bottom: DIS#1 taken on the left HRS, DIS#2 taken on the left HRS, and DIS#2 taken on the right HRS. All asymmetries shown here are blinded.	74
4-19 Pull distribution of the asymmetry for the global electron narrow trigger for $Q^2=1.1$ (GeV/c^2) (top) and 1.9 (GeV/c^2) (bottom), respectively.	75

List of Tables

4.1	Kinematics settings during the experiment. The spectrometer setting is shown as θ_0 (central angle) and E' (central momentum).	40
4.2	Corrections to the asymmetry due to all five beam positions that were monitored and evaluated using the dithering method.	44
4.3	Corrections to the measured raw asymmetries using the dithering method due to beam energy and position changes. The asymmetry uncertainty bars are statistical only.	44
4.4	Beam polarization.	48
4.5	PVDIS Q^2 uncertainty due to optics calibration for each HRS. The kinematics are ordered from left to right in the chronological order. .	58
4.6	Average electron detection efficiencies and pion rejection factors achieved through the lead glass (LG), the gas Cherenkov (GC) detectors and the combined performance. The error bars of the efficiency and the rejection factors are statistical only. The error bars for $f_{\pi/e}$ are shown separately for statistical uncertainties, systematic uncertainties due to our understanding of the rates, detector efficiencies and deadtimes, and systematic uncertainties due to day-to-day variations.	65
4.7	Average pion detection efficiencies and electron rejection factors achieved through the lead glass (LG), the gas Cherenkov (GC) detectors, and the combined performance. The error bars of the efficiencies and the rejection factors are statistical only. The error bars for $f_{e/\pi}$ are shown separately for statistical uncertainties, systematic uncertainties, and the systematic uncertainty due to day-to-day variations.	66

4.8 Simulated DAQ deadtime loss in percent for all kinematics and for both narrow (n) and wide (w) paths, along with the fractional contributions from the group, veto, and OR deadtimes. The uncertainty of the total deadtime is from the uncertainties of the group, veto and OR added in quadrature.	73
4.9 Preliminary asymmetries and corrections.	76

Chapter 1

Introduction

The Standard Model describes the fundamental interactions of particle physics. To date, almost all experimental tests described by the Standard Model have agreed with its predictions. However, people also believe that the Standard Model is only a part of a larger framework [4], primarily because it falls short of description at the energy region from the weak scale $M_{weak} \approx 250\text{GeV}$ up to the Plank scale $M_P \approx 2.4 \times 10^{18}\text{GeV}$. Parity-violating (PV) observables have played an important role in exploring the structure of the electroweak sector of the Standard Model. Thanks to the high luminosity, the use of polarized electron beam has played an increasingly important role in testing the Standard Model.

1.1 The Running of $\sin^2 \theta_w$

The weak mixing angle θ_w is an important parameter in the Standard Model. It describes the coupling strength of the $SU(2)_L$ and $U(1)_Y$ groups via the coupling constants g and g' . Electroweak radiative corrections induce a variation of the effective value of $\sin^2 \theta_w$ at momentum transfer Q^2 , with a minimum near the Z-pole at $Q^2 = M_Z^2$. This variation is known as “the running of $\sin^2 \theta_w$ ” and can be predicted by the Standard Model [5]. The test of this prediction requires a set of precision measurements at $Q^2 \ll M_Z^2$. The theoretical prediction of the running of $\sin^2 \theta_w$ and various experimental results are shown in Fig. (1-1).

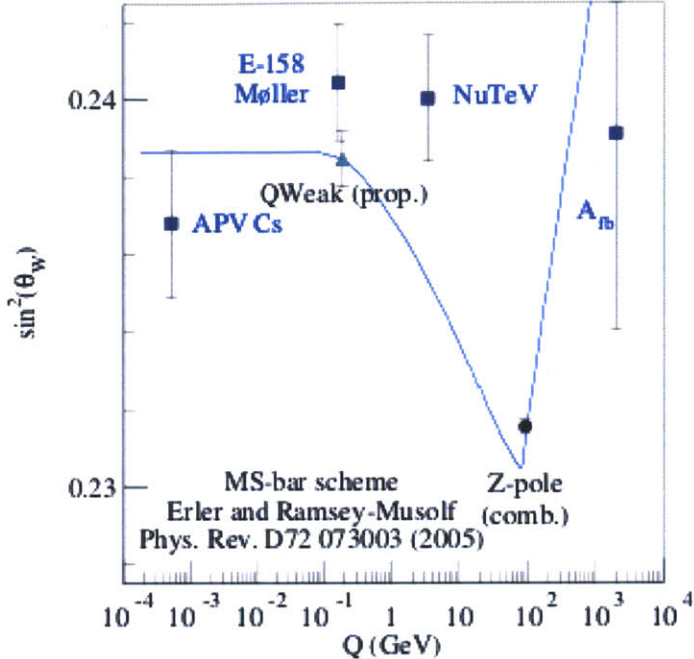


Figure 1-1: Theoretical curve of the running of $\sin^2 \theta_w$ and existing measurements from Cs APV, Fermilab NuTeV, SLAC E158 Møller. Also shown is expected uncertainty of the JLab QWeak experiment.

At the Z -pole, the value of $\sin^2 \theta_w$ has been measured, with remarkable precision, to be $\sin^2 \theta_w(M_Z) = 0.23120 \pm 0.00015$ [6, 7]. However, there is actually a three standard deviation inconsistency in measurements involving lepton and hadron electroweak couplings at the Z -pole. This indicates either some new physics beyond the Standard Model or some underestimated uncertainties in experiments [8].

In addition to the measurements at the Z -pole, there exists three precision measurements of $\sin^2 \theta_w$. The Møller experiment (E158) at SLAC extracted $\sin^2 \theta_w$ from the asymmetry $A_{L,R}$ of Møller scattering at $Q^2 = 0.026(\text{GeV}/c)^2$ [9]. The result is one standard deviation away from the SM prediction [10]. The second is the atomic parity violation (APV) on the cesium (Cs). An earlier measurement reported a two standard deviation result from SM prediction [11, 12]. After various atomic theory corrections associated with the extraction of $\sin^2 \theta_w$, the result has reasonably good agreement with the SM [13]. The third measurement was the NuTeV [14] at Fermilab, where the value of $\sin^2 \theta_w$ was extracted from the $\nu - N$ DIS cross sections on an iron target at $Q^2 \approx 20(\text{GeV}/c)^2$. The preliminary result was 3σ above the

SM value. However, possible hadronic effects including charge symmetry violation (CSV) [15], higher-twist effects, nuclear EMC effects of iron target were not taken into account. Hence, it is too early to say the result indicates new physics beyond the SM. The Qweak experiment [16] conducted in JLab Hall C also measured $\sin^2 \theta_w$ at $Q^2 \approx 0.03(\text{GeV}/c)^2$ using $e - p$ elastic scattering, but results are not yet published.

1.2 Weak Neutral Current Couplings at Low Q^2

The possible extension of the Standard Model can be explored by low energy precision tests of the electroweak sector of the Standard Model. One way is to measure weak neutral current (WNC) interactions at $Q^2 \ll M_Z^2$. While all of the low energy measurements shown in Fig. (1-1) measure $\sin^2 \theta_w$, they have sensitivity to different possible extensions of the Standard Model. In lepton-quark scattering on u and d quarks, there are six couplings [17]:

$$C_{1u} = g_A^e g_V^u = -\frac{1}{2} + \frac{4}{3} \sin^2 \theta_w \approx -0.19 \quad (1.1)$$

$$C_{1d} = g_A^e g_V^d = \frac{1}{2} - \frac{2}{3} \sin^2 \theta_w \approx 0.35 \quad (1.2)$$

$$C_{2u} = g_V^e g_A^u = -\frac{1}{2} + 2 \sin^2 \theta_w \approx -0.04 \quad (1.3)$$

$$C_{2d} = g_V^e g_A^d = \frac{1}{2} - 2 \sin^2 \theta_w \approx 0.04 \quad (1.4)$$

$$C_{3u} = g_A^e g_A^u = -\frac{1}{2} \quad (1.5)$$

$$C_{3d} = g_A^e g_A^d = \frac{1}{2}, \quad (1.6)$$

where taking approximately $\sin^2 \theta_w \approx 0.23$ ($Q^2 \ll M_Z^2$), g_A^e and g_V^e are the electron's axial and vector coupling, respectively, and $g_A^{u,d}$ and $g_V^{u,d}$ are the axial and vector coupling of u and d quark, respectively.

Of all the experiments searching for new physics beyond the Standard Model, the SLAC E158 Møller experiment is purely leptonic and is not sensitive to new interactions involving quarks, while APV and the Qweak experiment are semi-leptonic and can only access the weak couplings C_{1q} . Compared to C_{1q} , the weak coupling C_{2q} is poorly known. From existing data, $\Delta(2C_{2u} - C_{2d}) = 0.24$ ($Q^2 \ll M_Z^2$) [18]. This constraint is poor and must be improved in order to enhance sensitivity for exploring new physics beyond the Standard Model. e^-H parity violation deep inelastic scattering can provide precise data on $2C_{2u} - C_{2d}$, which is not accessible through other processes.

1.3 Parity Violation in Deep Inelastic Scattering and the Standard Model

Parity violation in deep inelastic scattering (PVDIS) was one of the first experiments to test the Standard Model. The first measurement of PVDIS at SLAC in the 1970's provided the value of $\sin^2 \theta_w \approx 1/4$ [19]. Since this experiment, parity violation has served as an important tool for testing the Standard Model and the structure of the nucleon. A number of facilities (JLab, SLAC, MIT-Bates, Mainz) have developed the capabilities of high luminosity to make studies of the weak neutral current and its coupling feasible. The Parity-violating asymmetry is proportional to the interference term between the weak and electromagnetic scattering amplitudes from which the weak neutral current can be accessed [20].

Electrons scatter from nuclear targets by exchanging either a virtual photon γ^* or a virtual Z^0 , as shown in Fig. (1-2). The four momentum transfer is $q = (\nu, \vec{q})$. For the case of inclusive measurement, only the scattered electron is detected. We denote the electron mass by m , $k = (E, \vec{k})$ and $k' = (E', \vec{k}')$ the initial and final

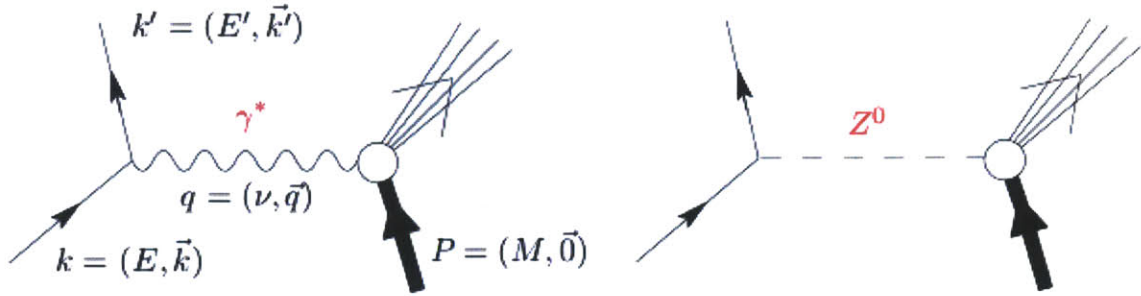


Figure 1-2: Tree-level Feynman diagrams for electron scattering.

electron four-momenta. The target has a mass M and its initial, final four-momenta are, respectively, $P = (E_t, \vec{P})$ and $P' = (E'_t, \vec{P}')$. In the case of a scattering with fixed target, one has $P = (M, \vec{0})$ in the laboratory frame. The Q^2 of exchanged virtual photon $\gamma^*(Z^0)$ is defined as $Q^2 \equiv -q^2$, where $q = k - k' = (\nu, \vec{q})$ is the four momentum transfer, ν is the energy transfer by the electron. The invariant mass is defined by

$$W \equiv \sqrt{M^2 + 2M\nu - Q^2}, \quad (1.7)$$

where M is the mass of the target (nucleus or nucleon) in the case of elastic scattering. In DIS, M denotes the mass of the nucleon. The Bjorken scaling variable x_B is defined as

$$x_B \equiv \frac{Q^2}{2P \cdot q} = \frac{Q^2}{2M\nu} \text{ for fixed target.} \quad (1.8)$$

When Q^2 is large enough, DIS can be interpreted as scattering off an asymptotically free quark inside the nucleon. The Bjorken variable x_B can be considered as the fraction of the nucleon's momentum carried by the struck quark. The DIS region is where the nucleon's partonic structure is explored.

For electron deep inelastic scattering from a nuclear target, the scattering amplitude \mathcal{M}_γ and \mathcal{M}_Z are the product of three terms: the currents of the electron, the propagator of the photon or the Z^0 and the currents of the hadron:

$$\mathcal{M}_\gamma = j_\mu \left(\frac{1}{q^2} \right) J^\mu \quad (1.9)$$

$$\mathcal{M}_Z = j_\mu \left(\frac{1}{M_Z^2} \right) J^\mu \quad (1.10)$$

The cross section for scattering longitudinally polarized right- or left-handed electrons from an unpolarized target is proportional to the square of the total amplitudes:

$$\sigma^r \propto (\mathcal{M}_\gamma + \mathcal{M}_Z^r)^2 \quad (1.11)$$

$$\sigma^l \propto (\mathcal{M}_\gamma + \mathcal{M}_Z^l)^2, \quad (1.12)$$

where \mathcal{M}_Z^r and \mathcal{M}_Z^l represent amplitudes for the right and left handed incident electrons, respectively. The parity violating asymmetry is thus

$$A_{sym} = \frac{\sigma^r - \sigma^l}{\sigma^r + \sigma^l} = \frac{(\mathcal{M}_\gamma + \mathcal{M}_Z^r)^2 - (\mathcal{M}_\gamma + \mathcal{M}_Z^l)^2}{(\mathcal{M}_\gamma + \mathcal{M}_Z^r)^2 + (\mathcal{M}_\gamma + \mathcal{M}_Z^l)^2} \approx \frac{\mathcal{M}_Z^r - \mathcal{M}_Z^l}{\mathcal{M}_\gamma}. \quad (1.13)$$

Therefore, the asymmetry is a ratio of amplitudes rather than the square of the ratio, which greatly enhances its sensitivity. The magnitude of the asymmetry can be estimated using $M_Z = 91.2\text{GeV}$ [21] based on the ratio of the propagators:

$$A_{sym} \approx \frac{Q^2}{M_Z^2} \approx 120 \text{ ppm at } Q^2 = 1(\text{GeV}/c)^2, \quad (1.14)$$

which is a large asymmetry for a parity violation experiment.

Following this formalism, the parity-violating asymmetry for scattering longitudinally polarized electrons from an unpolarized isoscaler target such as deuterium is [20, 22]

$$A_d = \frac{\sigma^r - \sigma^l}{\sigma^r + \sigma^l} \quad (1.15)$$

$$= - \left(\frac{3G_F Q^2}{\pi \alpha 2\sqrt{2}} \right) \frac{(2C_{1u} - C_{1d}) [1 + R_s(x)] + Y(2C_{2u} - C_{2d})R_v}{5 + R_s(x)}, \quad (1.16)$$

where the kinematic variable Y is defined as

$$Y = \frac{1 - (1 - y)^2}{1 + (1 - y)^2 - y^2 \frac{R_{LT}}{1 + R_{LT}}}, \quad (1.17)$$

with $y = \nu/E$ where $\nu = E - E'$ is the energy difference between an incident electron of energy E and the out going electron of energy E' . The ratio $R_{LT} = \frac{\sigma_L}{\sigma_T} \approx 0.2$ depends on x and Q^2 . The ratios $R_s(x)$ and $R_v(x)$ depend on the parton distribution functions:

$$R_s(x) = \frac{s(x) + \bar{s}(x)}{u(x) + \bar{u}(x) + d(x) + \bar{d}(x)} \quad (1.18)$$

and

$$R_v(x) = \frac{u_v(x) + d_v(x)}{u(x) + \bar{u}(x) + d(x) + \bar{d}(x)} \quad (1.19)$$

with $u_v(x)$ and $d_v(x)$ the valence quark distributions of u and d quarks, $u(x) = u_v(x) + u_{sea}(x) + \bar{u}(x)$, $d(x) = d_v(x) + d_{sea}(x) + \bar{d}(x)$, $s(x) = s_{sea}(x) + \bar{s}(x)$. $C_{1u(d)}$ represents the axial Z -electron coupling times the vector Z -u quark (d quark) coupling, while the $C_{2u(d)}$ is the vector Z -electron coupling times the axial Z -u quark (d quark) coupling.

At high x_B , one has $R_s \approx 0$ and $R_v \approx 1$, Eq. (1.16) reduces to[20, 22]

$$A_d = \left(\frac{3G_F Q^2}{\pi \alpha 2\sqrt{2}} \right) \left(\frac{1}{5} \right) [(2C_{1u} - C_{1d}) + Y(2C_{2u} - C_{2d})]. \quad (1.20)$$

Therefore it is clear that measurements at large Y will have more sensitivity to $(2C_{2u} - C_{2d})$.

1.4 Experiment Overview

JLab parity violating Deep Inelastic Scattering (PVDIS) experiment, E08-011, was completed in December 2009. The goal of this experiment was to measure the PVDIS

asymmetries to statistical precisions of 3% and 4% and with systematic uncertainties less than 3%, at $Q^2 = 1.1$ and 1.9 (GeV/c) 2 , respectively, and to extract the quark axial weak charge combination ($2C_{2u} - C_{2d}$) with the assumption that hadronic physics corrections are small. For this choice of kinematics, the expected asymmetries were 91 and 160 ppm, respectively, at the two Q^2 values. An event rate capability of up to 500 kHz was needed to achieve the required statistical precision. The experiment used a 100 μA electron beam with a polarization of approximately 90% and a 20-cm long liquid deuterium target. The standard High Resolution Spectrometers (HRS) in Hall A were used to detect the scattered electrons. The detector packages included the gas Cherenkov detector, two layers of lead-glass detectors and two scintillator planes. A new scaler-based fast counting DAQ was designed to achieve the required high rate capability. While the scaler-based DAQ only recorded events counting, the standard HRS DAQ recorded both fbTDC and ADC signal of all detectors. Hence the scaler-based DAQ was used for production counting mode and was supplemented by the standard HRS DAQ in the low-rate running to study the PID performance and deadtime effects that were used as a correction to the measured asymmetry. A general description of the Hall A standard apparatus is given in Chap. (2). In Chap. (3), the DAQ system is presented with an emphasis on its design scheme. The achieved PID performance, deadtime and the capability of measuring small asymmetries is discussed in Chap. (4). Finally, a summary and proposed future work is given in Chap. (5).

Chapter 2

Apparatus

2.1 Overview

The experiment took data in the Experimental Hall A at Thomas Jefferson National Accelerator Facility from Nov 2009 to Dec 2009. A schematic diagram of the experimental Hall A, which consists of the Hall A beam line elements, the deuterium target, and two High Resolution Spectrometers (HRS), is shown in Fig. (2-1).

The experiment used a longitudinally polarized beam with an average current of 105 μ A. Polarized electrons were excited from a super lattice GaAs photocathode by a circularly polarized laser [23, 24] at the injector of the CEBAF accelerator. The average beam polarization was 89%, which was measured periodically by Møller [3, 25] and Compton polarimeters [26, 27, 28]. A 20 cm-long unpolarized liquid deuterium target was used in this measurement. A series of beam diagnostic devices were used to measure the beam energy, position, and current. A luminosity monitor was located downstream on the beamline and was used to monitor target boiling effects. Most of the events in luminosity monitor are elastic. The asymmetry is in general proportional to Q^2 , hence the physics asymmetry detected by luminosity monitor is very small, of the order of 0.1 ppm. Therefore, the possible false asymmetries can be monitored at the 0.1 ppm level [2, 17]. The scattered electrons were detected by the two HRS in Hall A [3].

The experiment required measuring small asymmetries of order 100 ppm. The

techniques of precise asymmetry measurements have been successfully deployed in parity-violating electron scattering experiments at several facilities. The recent experiments at Jefferson Lab, such as HAPPEX [29, 30, 31, 32, 33] and PREX [34, 35], have achieved systematic uncertainties associated with helicity reversal at the 10^{-8} level. Most of experimental apparatus used by HAPPEX-III and PREX were also used by E08-011. The asymmetries measured in this experiment are at the order of 100 ppm with required accuracies of about 1 ppm, which is two orders-of-magnitude larger than the systematic uncertainty established in those recent experiments at JLab.

One important challenge of deep inelastic scattering experiments is the separation of scattered electrons from the charged pion background that arises from electro- or photo-production. While the standard HRS detector package and data acquisition systems provides a 10^4 pion rejection with approximately 99% electron efficiency, they are based on full recording of the detector signals and are limited to event rates up to 4 kHz [3]. This was not sufficient for the few-hundred kHz rates needed for this experiment. Thus custom electronics and a new DAQ was needed. We have built a scaler-based, cost effective counting DAQ, which can count at rates up to 1 MHz with hardware-based particle identification. The design of this new DAQ system is presented in Chap. (3).

2.2 Polarized Electron Beam

The CEBAF beam is highly polarized. The typical electron polarization at JLab is about 85% [3]. Polarized electrons are excited from a super lattice GaAs photocathode by a circularly polarized laser at the injector of the CEBAF accelerator [23, 24]. The sign of the laser polarization determines the electron helicity; helicity states are switched every 33 msec and each helicity state is referred to as a “window”. By reversing the sign of the laser circular polarization, the direction of the helicity at the target can be reversed rapidly [36]. Two “windows” of opposite helicity make a window pair. The first window of each helicity-sequence is generated using a pseudo-random

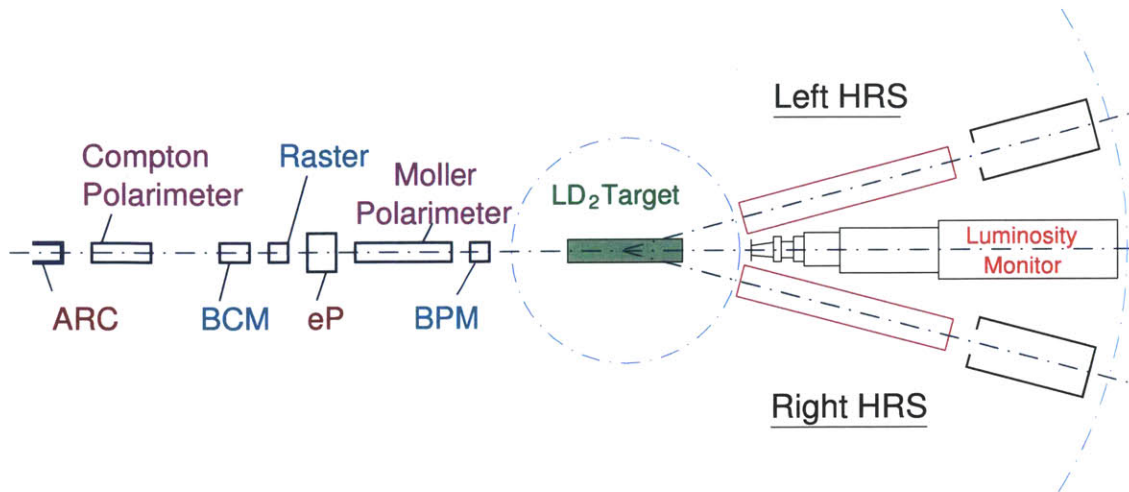


Figure 2-1: Floor plan of the PVDIS experiment in Hall A at Jefferson Lab. Beam enters from the left and scatters from a LD₂ target. The scattered electrons are detected in the two HRS (High Resolution Spectrometer) detector stacks. Reproduced from [1].

algorithm, and the second window of the helicity-pair is always the complement of the first (+- or --). During the E08-011 experiment, the sequence for beam helicity states followed a quartet structure, i.e. +---+ or -++--, and the sequence of the quartet was random. Approximately equal statistics were accumulated with opposite helicity signs for the measured asymmetry, which suppressed many systematic effects. Each helicity window (33.83ms) contained two full 60 Hz cycles of the power-line noise that averaged to zero [37].

Signals from the detectors in the spectrometers were integrated over the helicity window. The beam monitors, target, and detectors were designed so that the fluctuations such as electronic noise, detector pedestal fluctuations, beam fluctuations and target density fluctuations, between a pair of successive windows were controlled at a level much smaller than the counting statistics [2]. The statistical quality of data is shown in Sec. (4.9).

The integrated response of each beam monitor was digitized and recorded for each 33 msec window, while the scattered electrons were counted by the new DAQ. The raw asymmetry A_{raw} in each spectrometer arm was computed from the scattered flux recorded by the DAQ normalized to the beam intensity for each window pair.

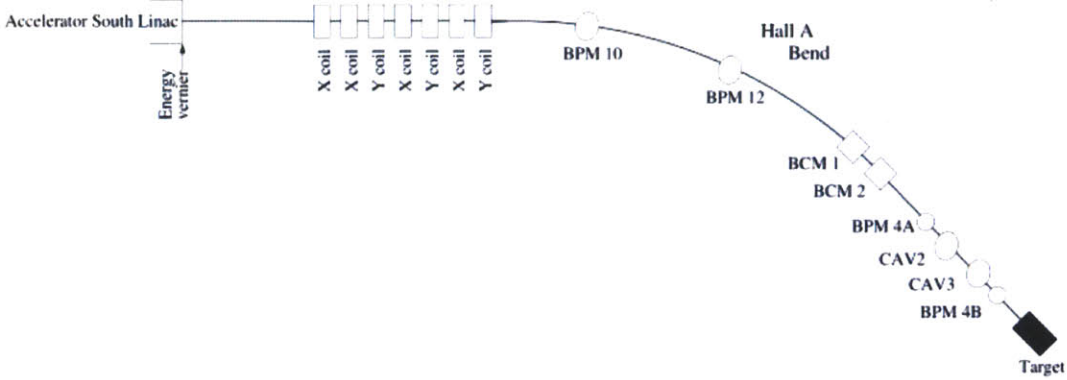


Figure 2-2: Locations of the BPMs and BCMs, along with the beam modulation (BM) coils used during E08-011. BPM4b and BPM4a were located 1.3 and 7.5m upstream of the target, respectively. BCM1 and BCM2 were separated by 3m. Reproduced from [2].

2.3 Beam Monitoring

Helicity-correlations in the beam properties such as energy and position are a primary concern for parity-violation experiments. E08-011 used the standard JLab beam current monitors (BCMs) [3] and beam position monitors (BPMs) [38] to measure the beam current and position respectively. The beam monitors were located at appropriate locations throughout the accelerator and the experimental halls of JLab. During the experiment, the monitors were constantly used to check for beam instabilities. The monitor signals were also used by automated feedback systems to maintain beam stability. Fig. (2-2) displays the locations of the BPMs and BCMs inside and at the entrance of Hall A that were used by E08-011.

2.3.1 Beam Current Monitor (BCM)

E08-011 used the BCMs developed locally at JLab to measure the beam current. The BCMs are resonant radio-frequency(RF) cylindrical high-Q waveguide cavities tuned to the frequency of the beam (1497 GHz) [3]. These BCMs provide non-interfering low-noise stable beam current measurements. They have a precision of 3.8 ppm at $100 \mu\text{A}$ over an integration length of 33.0 ms ($\sim 2.06 \times 10^{19}$ electrons). During experiment, BCM1 was used as the primary monitor for beam current measurement.

This experiment also used the “Unser” [39] to quantify the linearity of the beam monitors and to determine pedestals. The Unser is a parametric current transformer with its nominal response to current well determined. It was calibrated by passing a known current through a wire inside the beam pipe to measure its response. The Unser provided an absolute beam current measurement. However, its output drifts significantly on a time scale of several minutes [3]. Hence it was only used to calibrate the linearity of the beam monitors (BCM1), and not used for the primary beam current measurement.

In the analysis, BCM1 was used to normalize the detector signals for beam current fluctuations and to implement the beam current cuts. The BCMs were also used to monitor intrinsic beam noise by studying the differences in the beam asymmetry measured by different BCMs.

2.3.2 Beam Position Monitor (BPM)

The BPMs are wire stripline monitors composed of four antennas, X^+ , X^- , Y^+ and Y^- , placed symmetrically around the beam pipe. Each antenna provides a signal proportional to the beam position as well as intensity. In asymmetry analysis, the output from these stripline antennas were used to calculate the beam position as

$$x = \frac{X^+ - X^-}{X^+ + X^-} \times 18.76, \quad y = \frac{Y^+ - Y^-}{Y^+ + Y^-} \times 18.76, \quad (2.1)$$

where 18.76 is the distance in mm from the stripline axis center to the base of the antennas. The stripline antennas are situated at $\pm 45^\circ$ to the horizontal and vertical direction [38]. They were projected along the horizontal and vertical direction during analysis to determine the beam positions in the corresponding directions.

Numerous BPMs were read out from inside the hall, the arc, and the injector into the data stream. Most of these BPMs were recorded in the data stream for diagnostics during online and offline data analysis. BPMA-X,Y and BPMB-X,Y provided a projection of the beam position and angular fluctuations to the target. BPM12x is located at the arc and was used to monitor beam energy fluctuations.

The arc is located at the entrance of Hall A, where the beam is bent into the hall. This means that any beam energy fluctuations show up as horizontal beam position changes in the BPMs at the arc.

2.4 Target

The Hall A cryogenic target system [3] was used for this experiment. We used a 20-cm long deuterium cylindrical target cell for the main production data-taking, as well as auxiliary targets for evaluating backgrounds, studying the spectrometer optics, and checking beam centering. The target cell sits in an evacuated scattering chamber, along with subsystems for cooling, temperature and pressure monitoring, target motion, gas-handling, controls, and a solid and dummy target ladder.

The liquid deuterium loop was operated at a temperature of 22 K and a pressure of 25 PSIA (pound per square inch), leading to a density of about 0.0723 g/cm^3 . The Al-walled target cells were 6.48 cm in diameter, and were oriented horizontally, along the beam direction. The upstream window thickness was 0.071 mm, the downstream window thickness was 0.094 mm, and the side wall thickness was 0.18 mm. Also mounted on the target ladder were solid thin targets of carbon, and aluminum dummy target cells, for use in spectrometer and background studies, respectively.

The target was mounted in a cylindrical scattering chamber of 104 cm diameter, centered at the spectrometer pivot. The scattering chamber was maintained at a pressure 10^{-6} torr. The spectrometers view exit windows in the scattering chamber that were made of 0.406 mm thick Al plates.

To spread the heat load in the the target, the beam was rastered at 20 kHz by two sets of steering magnets 23 m upstream of the target. These magnets were able to deflect the beam up to ± 2.5 mm in x and y at the target. Local target boiling would manifest itself as an increase in fluctuations in the measured scattering rate, which would lead to an increase in the uncertainty of the pulse-pair asymmetries in the data, above that expected from counting statistics. Studies of the pulse-pair asymmetries for various beam currents and raster sizes were performed at a lower Q^2 and thus at

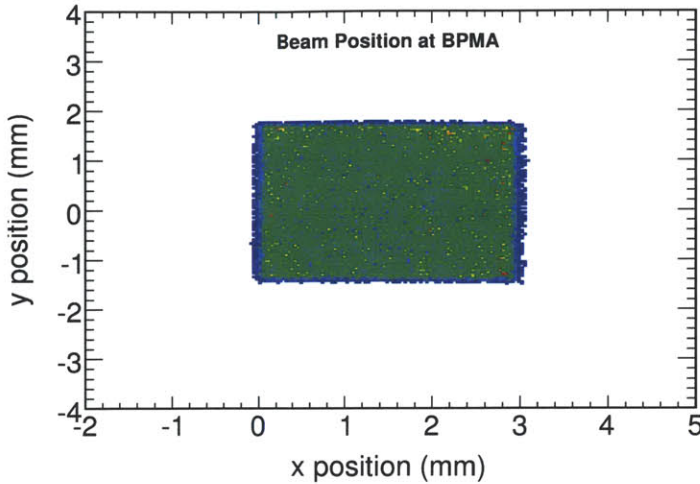


Figure 2-3: Rastered beam spot distribution at the target.

a higher scattering rate. During the experiment we used larger raster sizes for which there was negligible boiling effect; the beam was rastered to a $3 \times 3 \text{ mm}^2$ square spot at the target as shown in Fig. (2-3) .

2.5 Hall A Spectrometers

We used the standard Hall A High Resolution Spectrometers (HRS) to detect the scattered electrons. These spectrometers are designed for detailed investigations of the structure of nuclei and have high resolution to be able to isolate the different reaction channels in nuclei. Thus a clean comparison with theory can be achieved. They have a QQQDQ (Quadrupole-Quadrupole-Dipole-Quadrupole) magnet configuration [3]. The basic lay out is shown in Fig. (2-4). The $\pm 45^\circ$ vertically bending design includes a pair of superconducting $\cos(2\theta)$ quadrupoles followed by a 6.6 m long superconducting dipole magnet with focusing entrance and exit pole-faces, including additional focusing from a field gradients in the dipole. Following the dipole is a third superconducting $\cos(2\theta)$ quadrupole. The first quadrupole Q1 is convergent in the dispersive (vertical) plane. Q2 and Q3 are identical and both provide transverse focusing. With this setup, both spectrometers can provide a momentum resolution better than 2×10^{-4} [3].

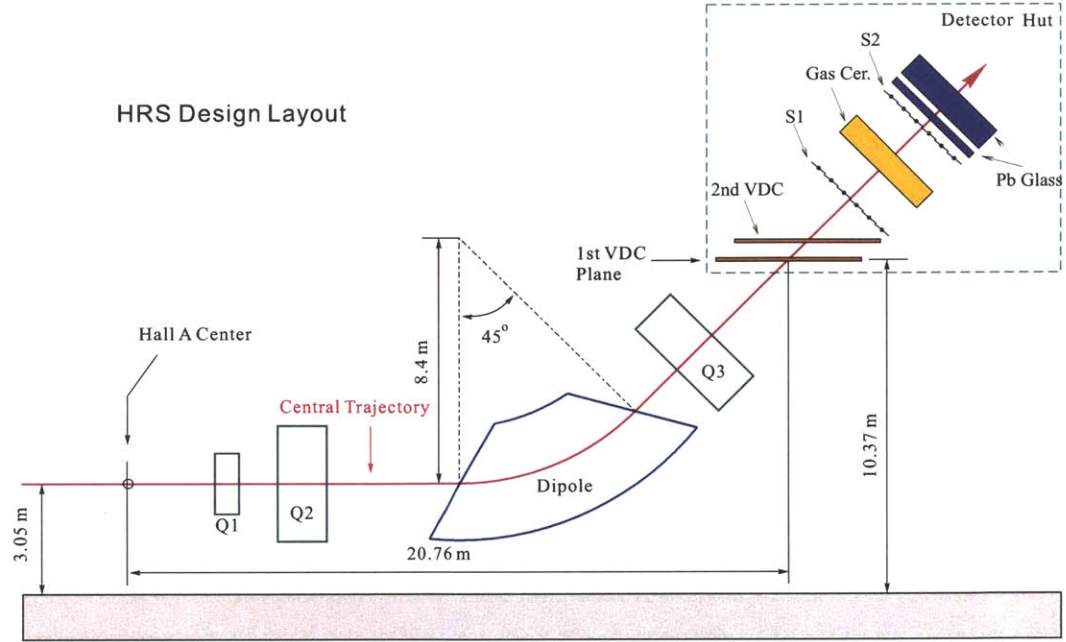


Figure 2-4: Schematic of a Hall A High Resolution Spectrometer and the detector package. Reproduced from [3].

The detector packages of the two spectrometers are designed to perform various functions in the characterization of charged particles passing through the spectrometer. These include: providing a trigger to activate the data-acquisition electronics, tracking (position and direction), timing, and identification of the scattered particles.

The detector package used in E08-011 to detect electrons and pions were:

- a set of two vertical drift chambers (VDCs) to provide tracking information
- two scintillator planes to provide basic triggers
- a CO₂ gas Cherenkov counter to provide particle identification (PID)
- two layers of lead glass for PID.

More details are given in the next chapter.

Chapter 3

A New Scaler-based Data Acquisition System (DAQ)

3.1 Motivation

One of the main challenges in deep inelastic scattering experiments is the separation of scattered electrons from the pion background. Charged pions may also have a parity-violation asymmetry when they are produced primarily from nucleon resonance decays. Assuming a fraction f of π^- contamination in the electron triggers and the pure electron fraction is $1 - f$, the measured asymmetry A_m is

$$A_m = f A_\pi + (1 - f) A_e \quad (3.1)$$

where A_e is the true electron asymmetry and A_π is the pion asymmetry. In order to achieve the experimental goals, one needs to both enhance the electron detection efficiency and minimize the pion contamination f to a negligible level. For the E08-011 experiment, the goal was to control f to the 10^{-3} level.

As described in Sec. (1.4), the two High Resolution Spectrometers were used to detect scattered events. While the standard HRS data acquisition system can provide a 10^4 pion rejection and 99% electron efficiency, they can only record event rates up to 4 kHz [3]. This was not sufficient for the 500 kHz rate requirement of the experiment.

Therefore, design of custom electronics and a DAQ were needed. In this section, we describe a scaler-based, cost effective counting DAQ which could record data up to 1 MHz and limit the pion contamination of the data sample to a negligible level of $f \approx 10^{-3}$.

3.2 DAQ Design

The new DAQ was designed to record data up to 1 MHz with low deadtime and PID performance of 10^4 pion rejection factor and 95% electron detection efficiency. As described in Sec. (2.5), we used the following detectors in the HRS to build the new DAQ:

- two scintillator planes
- a CO₂ gas Cherenkov detector
- a double-layer lead-glass detector
- the vertical drift chambers.

The two scintillator planes were used to provide the main trigger. The vertical drift chambers (VDC) were used to provide the position information for the studying of PID performance at every specific location over the whole focal plane. The VDCs were operated only during low beam current calibration runs and were turned off during high current production runs, since they can not endure the high event rates. Both the CO₂ gas Cherenkov and lead-glass detectors were used to provide particle identification (PID) information. Due to the high rates, the ADC signals of the gas Cherenkov and the lead-glass detector cannot be fully recorded. Hence, a hardware-based DAQ scheme was designed. The gas Cherenkov and lead-glass signals were passed through discriminators to form electron and pion triggers. By properly setting the discriminator thresholds, a hardware-based particle identification was realized. These triggers were then sent to scalers to count events. The scalers integrated counts

over the helicity window, which was held for 33 msec and flipped pseudo-randomly at 30 Hz as described in Sec. (2.2). Asymmetries were computed offline as

$$A = (n_R - n_L) / (n_R + n_L) \quad (3.2)$$

where $n_{R(L)}$ is the integrated rate of the triggers normalized to the integrated beam charge for the right(R) and left(L) handed helicity states of the incident electron beam.

As shown in Fig. (3-1), Each HRS has two layers of the lead-glass detector named as “preshower” and “shower” detector, respectively. All lead glass blocks in preshower and shower detectors were individually wrapped to prevent outside light. There were 48 blocks arranged in a 2×24 array in the preshower detector of the Right HRS. Each row of two blocks were read out by photo-multiplier tubes (PMTs). Therefore, the preshower detector had 48 output channels. In the shower detector of the Right HRS, there were 75 blocks arranged in a 5×15 array. The PMTs were attached to each block of the Right shower detector on one end only, giving 75 output channels. Unlike the different configuration of preshower and shower detectors in the Right HRS, the preshower and the shower detectors in the Left HRS were identical and both had 34 blocks arranged in a 2×17 array.

Due to the high rate, a large deadtime would be generated if signals from all blocks of the detectors were recorded. Therefore, as a compromise between the proposed high rates, the amount of electronics available and the deadtime, the lead-glass blocks in both the preshower and the shower detectors were divided into 6 (8) groups for the Left (Right) HRS, with each group consisting 8 blocks. Because the lead-glass detectors in the Left and Right HRS are different, the grouping scheme of the two spectrometers was also different, as shown in Fig. (3-1). Signals from the 8 blocks in each group were added using a custom-made analog summing unit called the “SUM8 module” before passing to the discriminators. Performance of various grouping configuration of both shower and preshower detectors were simulated and tested based on calibration data such that the best configuration was chosen with the maximum electron detection

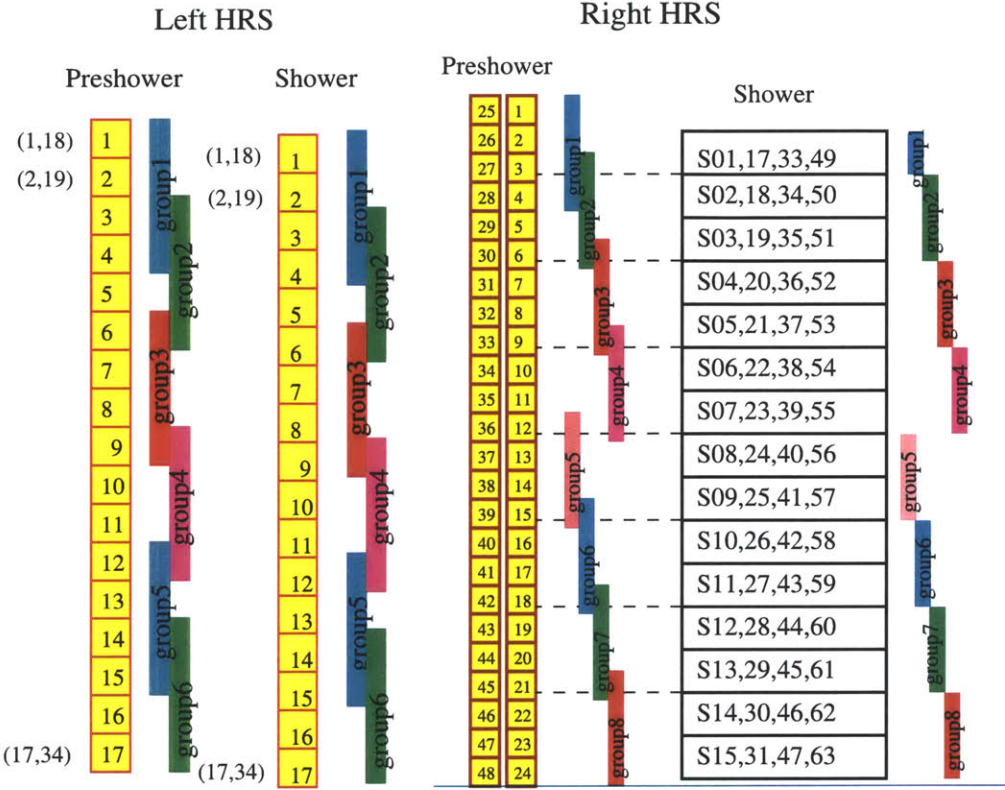


Figure 3-1: Grouping scheme (side-view) for the double-layer lead-glass detectors in the Left and the Right HRS. Index number of lead-glass blocks in both preshower and shower detector of Left and Right HRS is shown. Scattered particles enter the detector from the left. The colored vertical bars represent the range of each group.

efficiency. There were also overlapping blocks on adjacent groups in both preshower and shower detectors in Right and Left HRS.

A schematic diagram of the DAQ electronics for the Right HRS is shown in Fig. (3-2). Shower (SS) and preshower (PS) signals and their sums, called total shower (TS), signals were used to form preliminary electron and pion triggers. An event whose signal passed logical ANDs of the PS discriminator and the TS discriminator outputs was identified as a possible electron and formed the preliminary electron trigger. For pions, low threshold discriminators on the TS signal alone were sent to logical OR modules to produce preliminary triggers. In addition to the lead-glass signal, the gas Cherenkov (GC) and the “T1” signal [3] from scintillators (SC) were combined to provide additional background rejection via “VETO” gate. If a real electron passed the spectrometer, GC and T1 would produce a coincident signal

which formed an 150-ns wide electron VETO gate that allowed a final electron trigger to be generated from a preliminary electron trigger by the logical AND modules. On the other hand, each valid T1 signal without the GC signal would produce an 150-ns wide pion VETO gate that allowed an output to be formed by the logical OR modules from the preliminary pion triggers. The outputs of the logical AND and OR modules were called group electron and pion triggers, respectively. All 6 (8) group electron or pion triggers were then ORed together to form the global electron or pion trigger for the Left (Right) HRS. All group triggers and final global electron and pion triggers were counted using scalers. The timing of each group path was well aligned such that the event signals of overlapping part that was shared by two adjacent groups arrived at the final trigger simultaneously. Hence, only one copy of event signals of overlapping part was recorded by the DAQ and no double counting issue was caused.

Deadtime is the amount of time after an event during which the system is unable to record another event. Determining the deadtime is important in counting experiments, especially for measurements of small asymmetries. In order to monitor the counting deadtime of the DAQ, a “narrow” and a “wide” path of electronics were constructed. The only difference between these two paths was that the PS and the TS discriminator output widths of narrow path was 30 ns and that of wide path was set to be 100 ns. By studying the deadtime effects of these two paths, we confirmed our understanding about the system deadtime, which was analyzed in detail in Sec. (4.8).

The SUM8 modules mentioned above summed all lead-glass signals in a group and also provided two exact copies of the input PMT signals. One copy was sent to the parity scaler DAQ, and the other was sent to the standard HRS DAQ for calibration. During the experiment, data were occasionally taken at low rates using reduced beam currents with both DAQs functioning, such that a direct comparison of the two DAQs could be made. The vertical drift chambers were used during these low rate DAQ studies to provide tracking information for studying PID performance at each location over the whole focal plane. Signals from all PS, SH and TS discriminators, the T1 scintillator, the gas Cherenkov, and all electron and pion triggers were sent to Fastbus

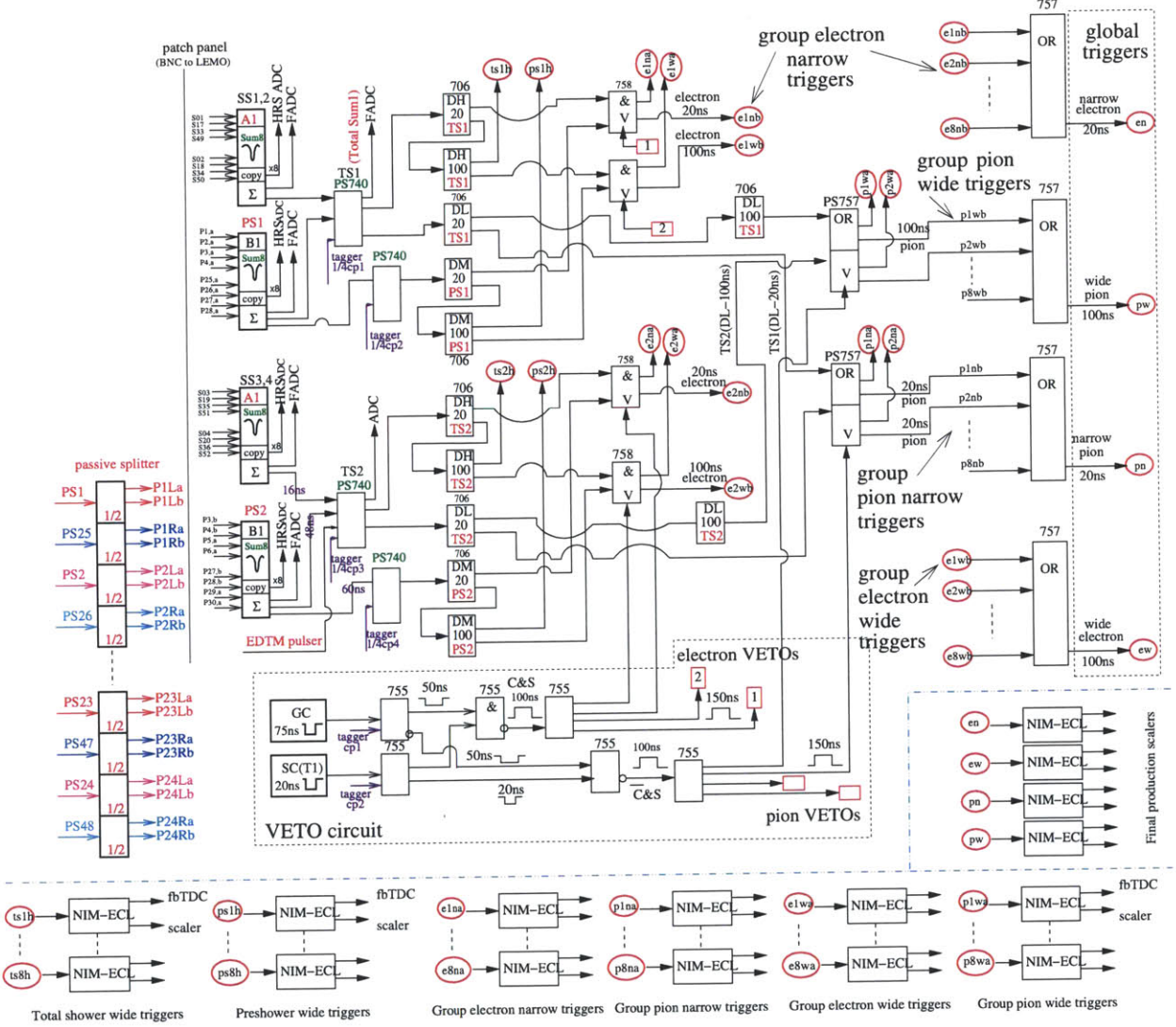


Figure 3-2: Electronics diagram for the Right HRS DAQ used by the E08-011 experiment. The Sum8's, discriminators and logic modules for two groups are shown, as well as the location of tagger signal inputs, setup of the VETO circuit using scintillator (SC) and gas Cherenkov (GC) signals, the logic units for combining triggers from all eight groups into final triggers, the counting scalers, and the monitoring fastbus TDCs. Electronics for the Left HRS was similar except for the grouping scheme.

TDCs (fbTDC) in the standard DAQ. Data from these fbTDCs were used to align timing of signals from all group paths. They were also used in the study of the PID performance of the lead-glass and gas Cherenkov detectors in the new DAQ.

Flash-ADCs (FADCs) were also used occasionally during the experiment to sample the full analog signals of the preshower and the shower SUM8 outputs, the intermediate logical signals of the DAQ, and the output electron and pion triggers. These FADC data provided a study of pileup effects and could also be used to confirm the deadtime simulation result.

Detailed DAQ analysis of PID performance and deadtime effect are described in Sec. (4.7) and Sec. (4.8), respectively.

THIS PAGE INTENTIONALLY LEFT BLANK

Chapter 4

Data Analysis

4.1 Overview of Data Taking

The experiment ran between October 26th and December 22nd, 2009. The main production kinematics were two deep inelastic scattering settings at $Q^2=1.1$ and 1.9 $(\text{GeV}/c)^2$ with a 6-GeV beam (referred to as DIS#1 and DIS#2, respectively). Data from four additional nucleon resonance settings RES#7, RES#3, RES#4 and RES#5 were also taken for the study of electromagnetic radiative corrections. We use convention introduced in [40] to define the different kinematics regions, where the resonance region usually refers to the region $1.2 < W < 2.0 \text{ GeV}/c^2$ and DIS regions is defined as $W > 2 \text{ GeV}/c^2$ and $Q^2 > 1.0 (\text{GeV}/c)^2$. The definition of invariant mass W and momentum transfer Q^2 are given in Sec. (1.3). An overview of all kinematics settings are shown in Table (4.1).

In this section, the procedure for data analysis of both the standard Hall A DAQ and the new parity DAQ are described. The general requirement on event selection is briefly discussed in Sec. (4.2), followed by asymmetry corrections due to fluctuations in the beam positions and energy in Sec. (4.3). The beam polarization is a major correction to the asymmetry and is presented in Sec. (4.4). Calibrations of the beam position and HRS optics are crucial for evaluation of the event kinematics. A full scale simulation of the HRS transport functions is presented in Sec. (4.5) and (4.6) to confirm our understanding of the kinematics resulting from these calibrations.

HRS	Kine#	$E_b(\text{GeV})$	θ_0	$E'(\text{GeV})$	$Q^2(\text{GeV}/c)^2$	x_B	$W(\text{GeV}/c^2)$
Left	DIS#1	6.0674	12.9°	3.66	1.10	0.24	2.07
	DIS#2	6.0674	20.0°	2.63	1.90	0.29	2.33
	Res#7	6.0674	15.0°	3.66	1.51	0.33	1.97
	RES#3	4.8674	12.9°	4.00	0.98	0.60	1.24
	RES#4	4.8674	12.9°	3.55	0.87	0.35	1.58
Right	DIS#2	6.0674	20.0°	2.63	1.90	0.29	2.33
	RES#5	4.8674	12.9°	3.10	0.76	0.23	1.86

Table 4.1: Kinematics settings during the experiment. The spectrometer setting is shown as θ_0 (central angle) and E' (central momentum).

Finally, corrections to the measured asymmetries due to various backgrounds are presented in detail in Sec. (4.7), (4.8) and (4.9).

4.2 Data selection and Cuts

Numerous cuts were imposed on the data to reject unusable or compromised data. Cuts were never made on any helicity-correlated (HC) asymmetries and were used to eliminate instabilities in the helicity signals, beam intensity, position, angle, energy, and instrument malfunctions. There were three distinct types of cuts: helicity sequence cuts, beam instability cuts and equipment malfunction cuts.

- The helicity sequence cuts discarded data with an incorrect helicity sequence. The helicity sequence used during E08-011 is described in Sec. (2.2). These cuts were implemented by comparing the helicity pattern recorded in the data with the expected helicity pattern. The Parity-Analyzer software (PAN) [41] was used for the data analysis. PAN ran a copy of the pseudo-random helicity generator algorithm identical to the one used to generate the beam helicity pattern. This helicity information was used by PAN to check for any missing or corrupt events in the helicity information read into the data stream. The helicity-pairs corresponding to the events that failed the helicity sequence cut were discarded. 25 events before and after each event that failed this cut were discarded as well.

- Beam instability cuts discarded data with periods of large beam instabilities that rendered the data unacceptable. These instabilities caused electron rate fluctuations at the detectors and monitoring devices, which increased the sensitivity of these devices to instrument non-linearities. Instrument non-linearities introduce false asymmetries and systematic uncertainties in the measured asymmetry. During experiment, beam was occasionally down and recovered afterward shortly. This beam down and recovery process was called a beam trip. For the PVDIS data, unacceptable beam conditions included periods of beam trips, fluctuations in the responses of the beam position monitors (BPM) of more than 200 nm and energy drifts resulting in the responses of BPM12x (BPM12y not used) of more than 200 nm. 10(400) events were discarded before(after) every beam trip and 10(40) events were discarded before(after) every unacceptable event resulting from beam instabilities other than the beam trips. The number of the discarded events were empirically determined to allow sufficient time for the detectors and monitors to fully recover from the instabilities, and avoid non-linearities.
- The equipment malfunction cuts discarded data corresponding to periods of equipment malfunctions. Periods of equipment malfunctions included periods of BPMs (specifically BPM12x) saturation, a non-functional HRS (one or both) and ADC internal errors. The data collected with periods of BPM12x saturation were discarded because BPM12x was the primary BPM used to correct for false asymmetries arising from random fluctuations in beam energy. Without reliable BPM12x data, such corrections for the effects of random fluctuations in energy could not be performed. Failure of one or more of the HRS magnets resulted in a non-functional HRS. Usually, only one of the HRS was non-functional at a time, while the other HRS was fully operational. During these instances, only the data collected in the functional HRS was retained. In instances when both HRSs were non-functional, no data were kept.
- All the low current ($<70\mu\text{A}$) data were discarded to ensure that most of the

data were collected at similar rates. The low current data made up a negligible fraction of the total data collected and contributed marginally to the statistics.

All cuts, except the HRS-nonfunctional cuts, were applied by PAN during standard analysis. PAN applied these cuts independently of one another. The periods of HRS non-functionality were manually tracked and the corresponding cuts were enforced after the standard PAN analysis.

4.3 Beam Corrections and Systematic Fluctuations

The sensitivity of the scattering cross section to random fluctuations in the beam position, angle and energy led to rate variations at the detectors that gave rise to false beam asymmetries. These fluctuations were the largest source of uncertainty beyond counting statistics in calculation of raw asymmetry. The false asymmetry was reduced by “dithering” techniques as follows.

We used the normalized flux $d_i \equiv D_i/I_i$ where D is the detected scattered flux of electrons, and I is the beam current, which were integrated over a whole helicity window independently. The raw asymmetry was then obtained by averaging of N measurements:

$$A_d \equiv \frac{d^+ - d^-}{d^+ + d^-} \equiv \frac{\Delta d}{2d} \quad (4.1)$$

$$\delta(A_d) = \sigma(A_d)/\sqrt{N}, \quad (4.2)$$

where + and – denote the two helicity states in a pair, $\Delta d = d^+ - d^-$ and $d = (d^+ + d^-)/2$ is the helicity-averaged normalized flux.

We desire that $\sigma(A_d)$ be dominated by counting statistics, but non-statistical instrumentation noise could also contribute to A_d . An example of possible non-statistical contributions is window-to-window relative beam intensity fluctuations,

$\sigma(A_I) \equiv \sigma(\Delta I/2I)$, which was on the order of 10^{-4} . This false asymmetry caused by beam intensity variation can be removed from the measured asymmetry:

$$A_d \approx \frac{\Delta D}{2D} - \frac{\Delta I}{2I} \equiv A_D - A_I, \quad (4.3)$$

which is Eq.(4.1) to first order.

Similarly, other non-statistical instrumentation noise such as random beam fluctuations in energy, position and angle can also affect $\sigma(A_d)$ and the corrections can be made as follows:

$$A_d^{corr} = A_D - A_I - \sum_j \beta_j (\Delta M_j). \quad (4.4)$$

where M_j are a set of five BPMs (BPMA-X,Y, BPMB-X,Y and BPM12x) that span the parameter space of energy, position and angle on target, and $\beta_i \equiv \partial D / \partial M_i$ is the detectors response to the variation of beam parameters.

During the data taking, the beam position, angle, and energy were modulated periodically and intentionally. The energy of the beam was varied by applying a control voltage to a vernier input on a cavity in the accelerator's South Linac. The beam positions and angles were modulated using seven coils in the Hall-A beamline that are located upstream of the dispersive arc [29, 30, 31, 32]. The resulting variations in the asymmetries were measured for each of the five BPM positions so that the value of β_j can be calculated. These modulation periods were excluded from the production data sample in the data selection stage, but the appropriate corrections were made to the measured asymmetries using the measured β_j and beam variations ΔM_j measured during the production data sample. This is what we call the "dithering" method for the beam corrections.

We found that the fluctuation in the beam positions varied between 1 and 10 μm and the fluctuation in the beam energy asymmetry was typically less than 10^{-5} for these variations. For most of the running conditions, $A_d^{corr} \approx A_D \approx 100 \text{ ppm}$, and all corrections were negligible compared to the uncertainties from the counting statistics. Overall, the uncertainty in the asymmetry measurement was dominated by

Monitor	Left DIS#1 Correction (ppm)	Left DIS#2 Correction (ppm)	Right DIS#2 Correction (ppm)
BPM4AX	0.025	0.141	0.018
BPM4AY	0.058	0.137	0.001
BPM4BX	0.025	0.131	0.023
BPM4BY	0.066	0.072	0.006
BPM12x	0.002	0.008	0.002
Total	0.095	0.247	0.030

Table 4.2: Corrections to the asymmetry due to all five beam positions that were monitored and evaluated using the dithering method.

	Left DIS#1	Left DIS#2	Right DIS#2
A_{raw} (ppm)	-78.44 ± 2.68	-140.49 ± 10.43	-139.87 ± 6.58
A_{dit} (ppm)	-78.45 ± 2.68	-140.30 ± 10.43	-139.84 ± 6.58
Correction (ppm)	0.01 ± 0.10	-0.19 ± 0.25	-0.03 ± 0.03

Table 4.3: Corrections to the measured raw asymmetries using the dithering method due to beam energy and position changes. The asymmetry uncertainty bars are statistical only.

the counting statistics in the scattered electron flux. Table (4.2) shows the corrections due to fluctuations in five BPMs by using the dithering method. The measured and the dithering-corrected asymmetries and their differences are shown in Table (4.3).

4.4 Beam Polarimetry

The experimental asymmetry A^{exp} is related to the corrected asymmetry by

$$A^{exp} = A_d^{corr} / P_e \quad (4.5)$$

where P_e is the beam polarization. Two beam polarimeters techniques were used for E08-011: a Møller polarimeter and a Compton polarimeter.

4.4.1 Møller Polarimeter

The Hall A Møller polarimeter [3, 25] measures the beam polarization by measuring the asymmetry in $e - e$ scattering. Its cross section depends on the beam and target polarizations, P^{beam} and P^{target} , as well as on the analyzing power A_i of Møller

scattering,

$$\sigma \propto \left(1 + \sum_{i=X,Y,Z} (A_i \cdot P_i^{target} \cdot P_i^{beam}) \right), \quad (4.6)$$

where $i = X, Y, Z$ defines the projections of the polarizations. The analyzing powers A_i depend on the scattering angle θ_{CM} in the center-of-mass (CM) frame and are calculable in QED [25]. Assuming that Z is parallel to the beam (longitudinal direction), and X-Z is the scattering plane

$$A_Z = -\frac{\sin^2 \theta_{CM} (7 + \cos^2 \theta_{CM})}{(3 + \cos^2 \theta_{CM})^2} \quad (4.7)$$

$$A_X = -A_Y = -\frac{\sin^4 \theta_{CM}}{(3 + \cos^2 \theta_{CM})^2}. \quad (4.8)$$

The absolute values of A_Z reach the maximum of $7/9$ at $\theta_{CM} = 90^\circ$. A beam polarization transverse to the scattering plane also leads to an asymmetry, though the analyzing power is lower: $A_X = -A_Y = A_Z/7$. The main purpose of the polarimeter is to measure the longitudinal component (Z direction) of the beam polarization.

The polarimeter target is a ferromagnetic foil that is magnetized in a magnetic field along its plane. The target foil can be oriented at various angles with respect to the beamline. The beam polarization may have a transverse component (X,Y direction), which would couple to the transverse component of the target polarization. The way to cancel the influence of this transverse component is to take an average of the asymmetries measured at two opposite target angles, for instance, $(\pm 20^\circ)$. At a given target angle, two sets of measurements with oppositely-sign target polarizations are made, which cancels some false asymmetries such as beam-current asymmetries.

The Møller-scattered electrons are detected in a magnetic spectrometer consisting of three quadruples and a dipole. The detector consists of scintillators and lead-glass calorimeter modules in two arms in order to detect the electrons in coincidence. The total systematic uncertainty that can be achieved is 3.4% which is dominated by uncertainty in the polarization of the foil [25].

4.4.2 Compton Polarimeter

The Compton polarimeter provides a continuous, non-invasive measurement of the beam polarization using the well-known QED Compton scattering cross section [26, 27, 28]. The polarization is extracted from the measurement of the counting rate asymmetry for opposite beam helicities in the scattering of a circularly polarized photon beam off the electron beam

$$A^{exp} = (N^+ - N^-) / (N^+ + N^-) \quad (4.9)$$

where A^{exp} is the experimental Compton scattering rate asymmetry and $N^+(N^-)$ refers to Compton counting rates for right (left) electron helicity, normalized to the beam intensity. This asymmetry is related to the electron beam polarization via

$$P_e = \frac{A^{exp}}{P_\gamma A^{th}} \quad (4.10)$$

where P_γ is the photon polarization and A^{th} is the theoretical Compton scattering rate asymmetry at 100% photon and electron polarizations.

The Compton polarimeter consists of a magnetic chicane, a photon source, a photon detector, and an electron detector. The electron beam is deflected vertically by the four dipoles of the chicane and crosses the photon beam at the Compton Interaction Point (CIP). After interaction, the back-scattered photons are detected in the calorimeter photon detector and the electrons in the silicon strip electron detector [28]. Electrons that do not interact exit the polarimeter and reach the target in the hall. The circular polarization state of the photon beam, P_γ , is determined by a quarter-wave plate located outside the cavity on the photon beam line [26, 27].

4.4.3 Beam Polarization Results

During our experimental run, the Møller polarimeter ran the entire time, while the Compton polarimeter initially suffered from a high background and produced good results only in the last three weeks of the run. Fig. (4-1) shows the Møller po-

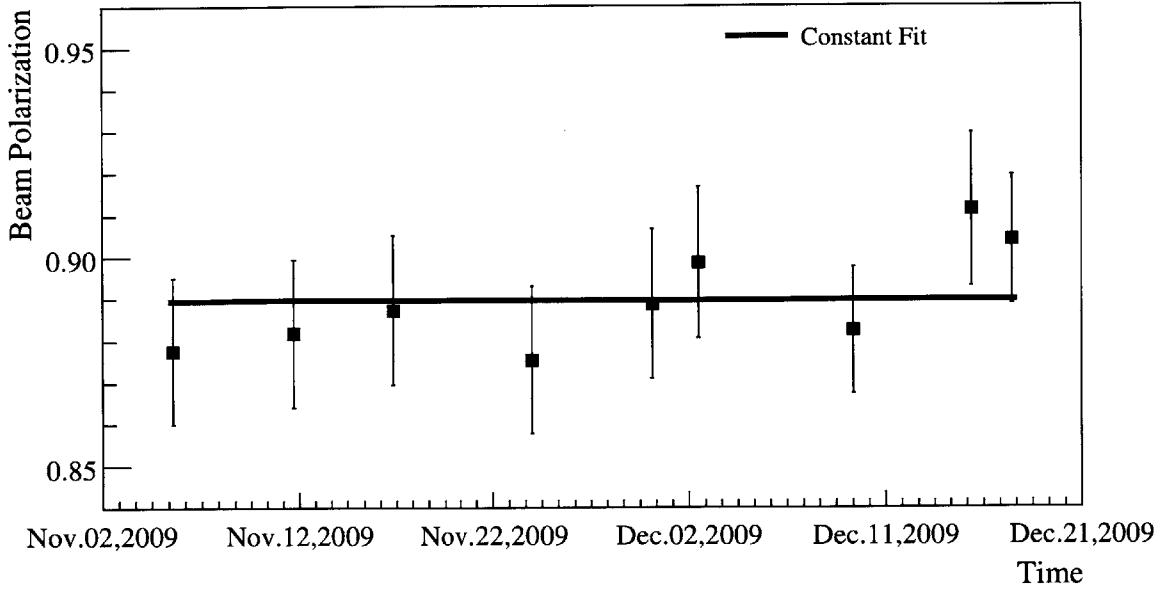


Figure 4-1: Polarization history from the Møller polarimeter measurements. The error bars include systematic uncertainties.

larimetry measurements during our experiment, and Fig. (4-2) shows the Compton measurements together with Møller measurements that were taken during the same time period.

The average beam polarization is 88.97% for Møller and 89.45% for Compton. The way that we apply the beam polarization correction is as follows:

1. The beam polarization is corrected run by run.
2. When there's no Compton measurements (before Dec 2), only Møller results are used. Each Møller data point is used for the consecutive days until the next data point is available.
3. When there are both Compton and Møller results (after Dec 2), the Compton data are averaged first and then this average is averaged with each Møller point. These results are applied for the correction in the same way as item 2.

The average run-by-run beam polarization corrections are shown in Table (4.4) for the different kinematics.

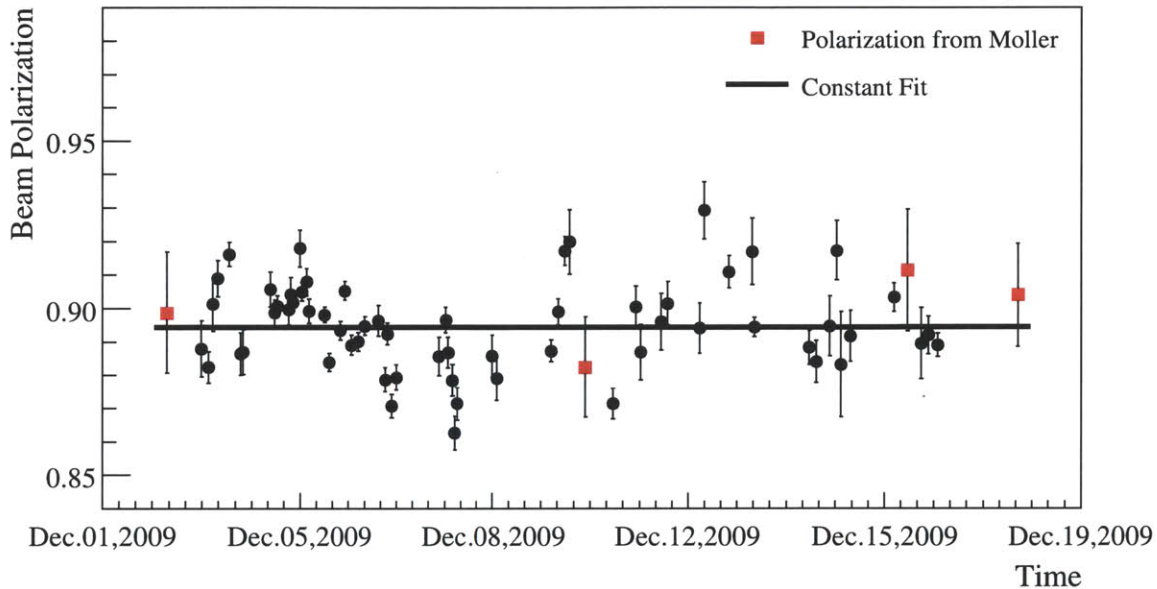


Figure 4-2: Polarization history from the Compton polarimeter measurements (round points), together with Møller measurements (square points) during the same time. The error bars for Compton are statistical only, while Møller includes systematic uncertainties.

	Left Kine 1	Left Kine 2	Right Kine 2
Polarization	88.18%	89.29%	88.73%
Uncertainty	1.76%	1.19%	1.50%

Table 4.4: Beam polarization.

4.5 Beam Position Calibration

The absolute beam position on the target affects the evaluation of kinematics (Q^2 , W , x) of each event.

The beam position information for each event must be obtained from the raster current rather than the delayed BPM information, which is recorded for that event. Calibration of the beam position from the raster current information can be described by offsets and the ratio of their RMS values:

$$\text{bpm offset } x = \langle \text{bpm } x \rangle + \langle \text{raster current } x \rangle \times \frac{\sigma_{\text{bpm } x}}{\sigma_{\text{raster current } x}} \quad (4.11)$$

$$\text{bpm offset } y = \langle \text{bpm } y \rangle + \langle \text{raster current } y \rangle \times \frac{\sigma_{\text{bpm } y}}{\sigma_{\text{raster current } y}} \quad (4.12)$$

Fig. (4-3) shows the reconstructed beam position before and after the BPM calibration. The blue line is the beam position as determined by the BPMs, and the red line is the beam position as determined by the raster current.

4.6 Calibration of the HRS Optics

To accurately determine the kinematics (Q^2 , W , x) of each event, one must reconstruct the scattering angle and scattered electron's momentum from the particle trajectory. In this section, the VDC timing calibration is described first, which affects the precision of particle track determination. Then, the procedure to calibrate the position, the scattering angle and the scattered electron's momentum are discussed in detail. Finally, the uncertainty in the event's kinematics as a result of the calibration are presented.

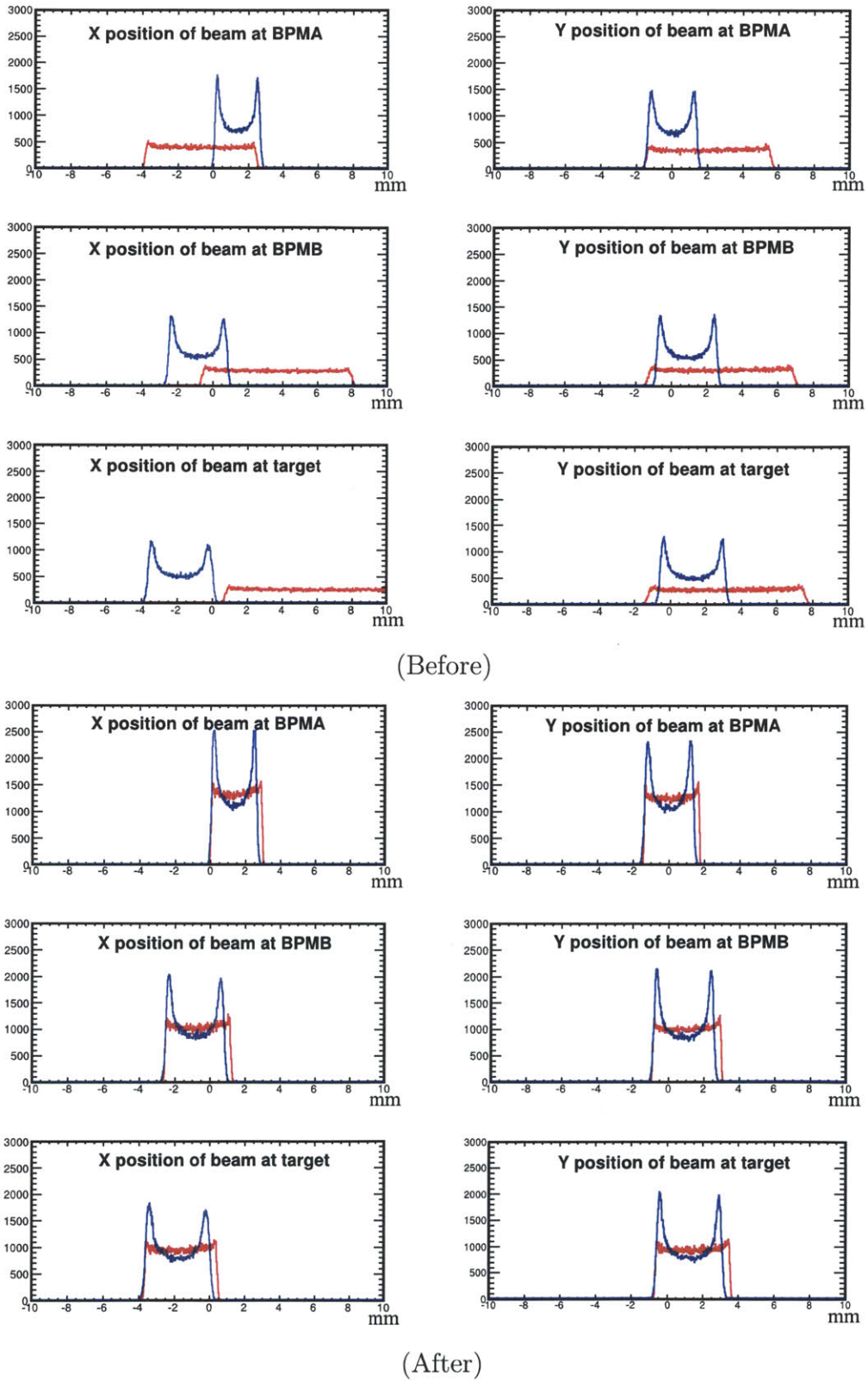


Figure 4-3: Beam position reconstruction before (top) and after (bottom) BPM calibration. The blue lines are the beam positions determined by the BPMs, and the red lines are the beam positions determined by the raster current.

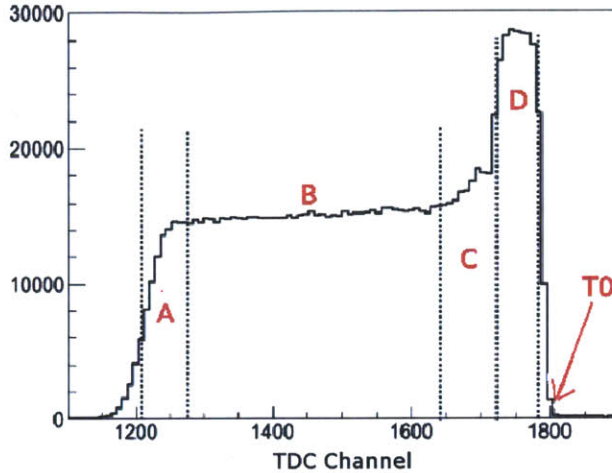


Figure 4-4: A drift-time Spectrum of a VDC plane.

4.6.1 VDC Timing Calibration

The TDCs were operated in the common-stop mode and larger TDC values correspond to shorter drift times. A typical TDC spectrum of a wire plane is shown in Fig. (4-4) where the drift times of all the wires are plotted. The various regions in the spectrum can be understood as follows:

- **Region A:** This is a region that corresponds to the particles with trajectories far away from the drift cell and falling out of the possible cell timings. Statistical fluctuation of gas ionization also smears the slope.
- **Region B:** This region has all the field lines parallel and hence the drift velocity of the electrons is constant.
- **Region C:** In this region, the field lines begin to change from parallel to quasi-radial closer to the sense wires.
- **Region D:** This region corresponds to a region very close to the sense wires where the drift velocity of the electrons increases drastically.

In order to use the VDC drift time spectrum to reconstruct track information, the reference timing T_0 for all wires needs to be calibrated to one common reference time so that the various timing offsets due to cable lengths and signal processing times

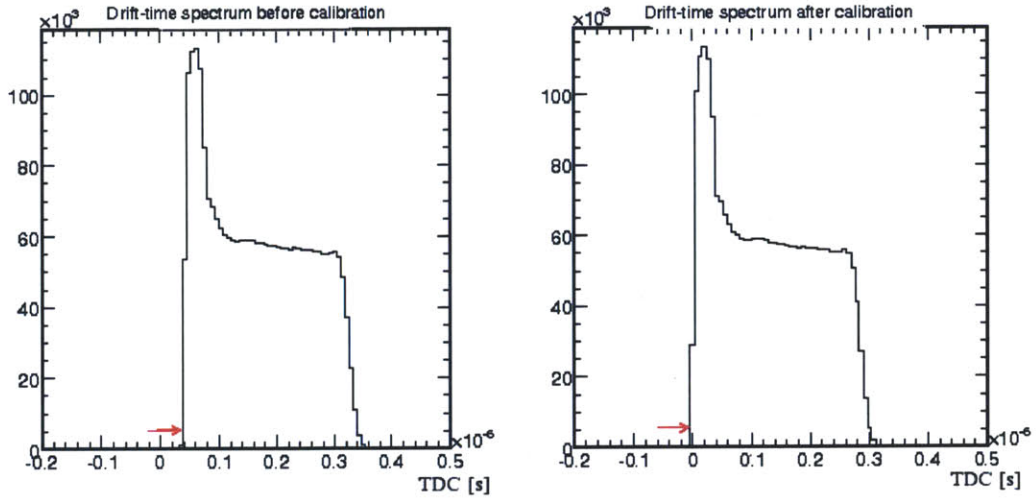


Figure 4-5: Drift-time spectrum of all wires in VDC U1 plane before (left) and after (right) T_0 timing correction.

could be eliminated. The calibration procedure involved the determination of T_0 for all wires in each VDC plane (U1, U2, V1, V2). T_0 for each wire was determined by differentiating the region of a short drift time around channel 1800 and looking for the maximum slope. Once the maximum slope was calculated, it was extrapolated to the horizontal channel axis and the point of intersection was determined as T_0 . Each wire in the four VDC planes was timed and the reference T_0 was chosen to be 0 ns in the corrected timing spectrum. Fig. (4-5) shows the drift-time spectrum of all wires in the VDC U1 plane before and after T_0 timing.

4.6.2 Optics Matrix Calibration and Systematic Uncertainties

Once the VDC timing is calibrated, the VDCs can provide precise information on the hit positions and angles at the focal plane ($x, \theta, y, \phi, \delta$), which further determines the particle trajectory. This information is used to reconstruct the interaction variables at the target. This is done by determining the inverse of the HRS optical transport matrix. In practice, instead of a matrix operation, a set of tensors up to 5th order

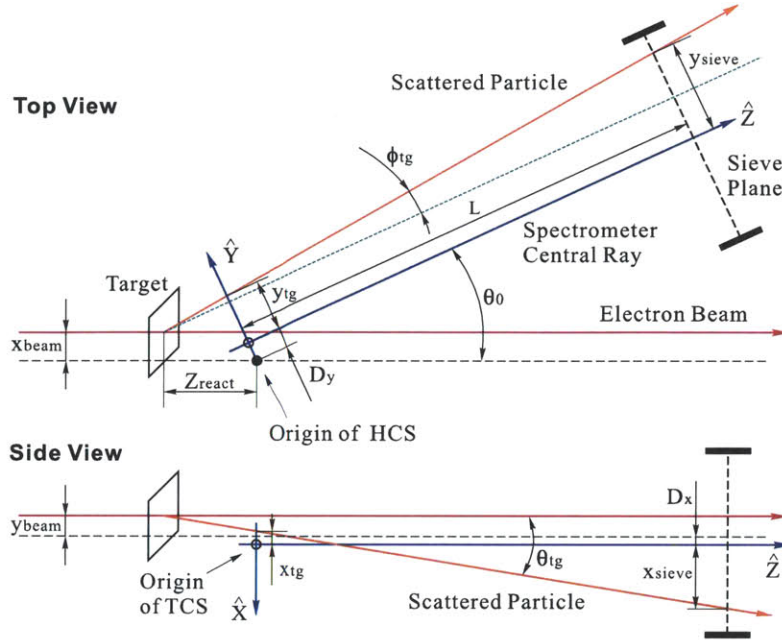


Figure 4-6: Target coordinates of the scattered event and the coordinates of the sieve plane (topview). ϕ_{tg} is the in-plane angle with regard to the spectrometer central ray and θ_{tg} is the out-of-plane angle. The y-sieve axis is pointing to the left of the spectrometer entrance and the x-sieve axis points vertically down. Reproduced from [1].

are used to calculate the target quantities from the focal plane variables.

The target coordinates of the scattering event, $(x_{tg}, y_{tg}, \theta_{tg}, \phi_{tg})$, are defined in the target coordinate system (TCS) [42] with respect to the spectrometer central ray direction, see Fig. (4-6). Here the angles θ_{tg} and ϕ_{tg} refer to the angles of the vertical and horizontal trajectory relative to the HRS central ray. The spectrometer pointing D is the distance at which the spectrometer misses the Hall center in the direction perpendicular to the spectrometer central ray. For optics studies, a sieve plane is located at the entrance of the spectrometer. The drift distance from the target center to the sieve plane is $L = 1.12$ m. The particle hit position and the angles at the sieve plane can be directly calculated from the focal plane variables.

In general, the optics calibration can be divided into three calibration steps:

- 1) Calibration of the interaction vertex position along the target, Z_{react} , which is related to y_{tg} in the TCS as well as the mis-pointing D of the spectrometer. The vertex calibration is done by taking calibration data on a multi-foil carbon target with

well known foil positions. The foil position can thus be determined from data using the HRS optics matrix, the focal plane variables, and D. The calibration precision on Z_{react} in the direction perpendicular to the spectrometer central ray is determined by

$$\Delta(z_{react}\sin\theta_0) = \sqrt{\Delta D^2 + (\Delta z_{foil}\sin\theta_0)^2 + (\Delta z_{data}\sin\theta_0)^2}, \quad (4.13)$$

where $\Delta z_{foil} = \pm 2.5\text{mm}$ is determined by the knowledge of the actual foil position which is dominated by possible shifts of the target ladder during the target cool-down. The precision of D is obtained from spectrometer pointing survey (typical precision is $\pm 0.5\text{ mm}$). If a survey is not available and hence the mis-pointing D is unknown, the optics matrix of a previous similar spectrometer angle setting is used. Then by comparing the carbon foil positions reconstructed by this approximate optics matrix with the target nominal positions, a global shift of all foil positions is observed which can be used to derive the value of mis-pointing D. By fine tune the mis-pointing D, a $\pm 0.5\text{ mm}$ uncertainty from the Z_{react} reconstruction can be achieved. Δz_{data} is determined from the resolution and accuracy achieved in the multi foil positions reconstructed from data (typically $\pm 0.1\text{ mm}$ if no obvious discrepancy is observed). For spectrometer mis-pointing D, in the case that neither carbon foil data nor a survey is available, ΔD is taken to be $\pm 5\text{ mm}$, which is the limit of how much the spectrometer can physically miss point to the Hall center.

2) Calibration of the scattering angle θ_{tg} and ϕ_{tg} . This is done by inserting the so-called “sieve slit” plate, a 0.5-mm thick tungsten plate with an array of pinholes at the entrance of the spectrometer. Reconstruction of the hole position precisely determines the angle elements of the spectrometer optics matrix. The calibration precision is determined by the knowledge of the x_{sieve} and y_{sieve} hole positions with regard to the center of the spectrometer and the resolution and accuracy in the reconstructed hole positions ($\pm 0.1\text{ mm}$ if no obvious discrepancy is seen).

The most straightforward way to determine x_{sieve} and y_{sieve} is by a survey of the sieve slit plate with typical precisions of $\pm 0.5\text{ mm}$ for both directions. From past experience it was found that if no survey is available and there is no work done on

the sieve slit plate (such as taking it off and putting it back on the HRS entrance), the horizontal position y_{sieve} is highly reproducible to ± 0.1 mm, and thus survey results from previous experiments can be used with this additional uncertainty added. The vertical position x_{sieve} is reproducible to ± 0.5 mm due to the fact that this is the direction in which the sieve plate is moved into or out of the HRS entrance. If no sieve slit data was taken, the angle calibration of a preceding experiment can be used based on the high reliability of the HRS. In this case, an additional ± 0.5 mrad of uncertainty is added in both directions to account for possible changes in the optics.

3) Momentum calibration: The most precise way to calibrate momentum is to use the elastic data from a carbon target or the proton in a water target. With a water target, the relative momentum $\delta = dp/p$ with p the HRS central momentum setting can be determined to $\pm 1 \times 10^{-4}$. A water target calibration was performed for the preceding experiment (HAPPEX-III) which we could use. Due to the high stability of the HRS magnets and transport system, one expects an uncertainty of $\delta = \pm 5 \times 10^{-4}$.

The three calibration steps described above are in general treated as decoupled from one another, i.e., matrix elements related to position reconstruction have little dependence on those related to angle reconstruction, and vice versa. For all calibration methods above, the optics tensor coefficients are determined by a χ^2 minimization procedure in which the events are reconstructed as close as possible to the known position of the corresponding foil target or the sieve-slit hole.

4.6.3 Optics Calibration Results

In the E08-011 experiment, there were a total of seven kinematics settings which are listed in Table 4.1. Either vertex or angle calibrations, or both, were carried out for all settings except RES#7 and RES#7b. Typical examples of the vertex and angle calibration results of Left DIS#1 are shown in Fig. (4-7) and Fig. (4-8) receptively.

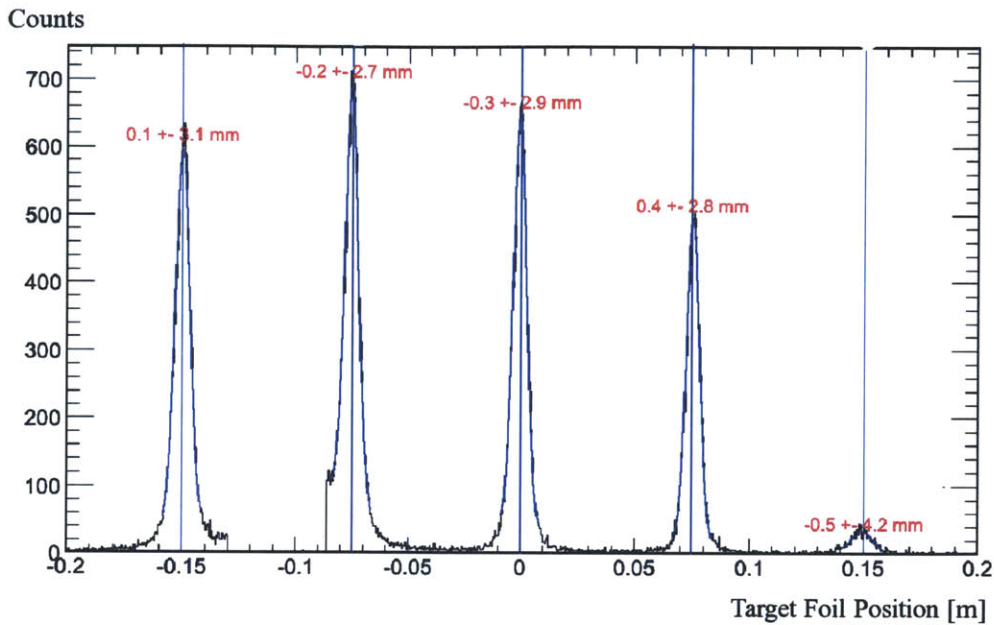


Figure 4-7: Vertex reconstruction of left kinematics 1. The numbers shown in the plot are the difference between the reconstructed target position and target survey position.

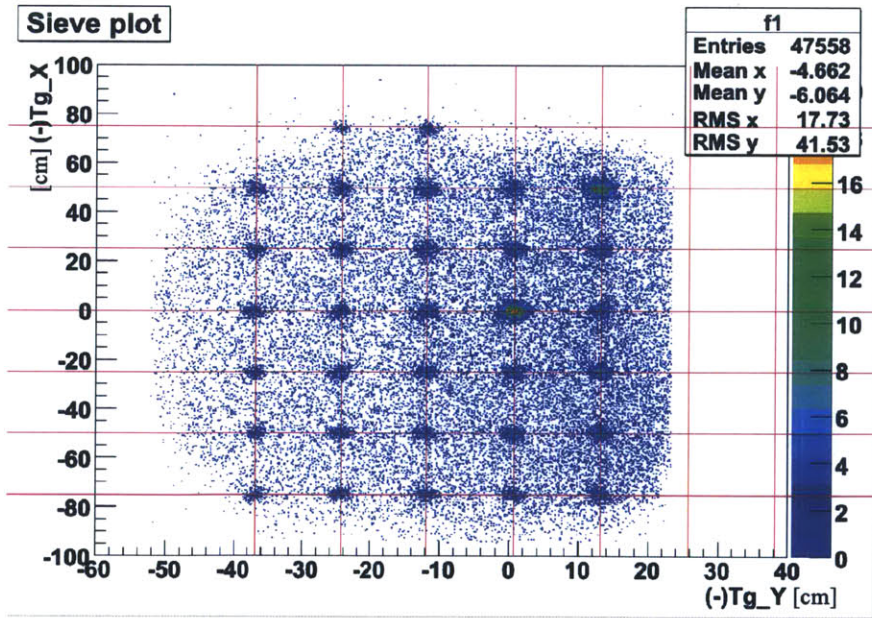


Figure 4-8: Sieve reconstruction of left kinematics 1. Grid lines represent the sieve-hole survey position.

4.6.4 Q^2 Uncertainties

The uncertainty related to each calibration is described above. For some settings, one might have both angle and vertex calibrations (Left RES#3 and RES#4), or only the vertex but not the angle calibration (Left DIS#1, Left DIS#2, Right DIS#2, Right RES#5), or neither (Left RES#7 and RES#7b). The total uncertainty on the scattering angle is

$$\Delta\theta \approx \sqrt{(\Delta D/L)^2 + (\Delta z_{data} \sin\theta_0/L)^2 + (\Delta z_{foil} \sin\theta_0/L)^2 + (\Delta\phi_{tg})^2}, \quad (4.14)$$

where the drift distance $L = 1.12\text{m}$.

For both vertex and angle calibrations, the HAPPEX-III experiment ran immediately before the PVDIS experiment reported here, and the HAPPEX-III optics database and some survey results were used for some of our kinematics settings. Taking all uncertainties into account, the relative uncertainty in Q^2 for each kinematics due to HRS optics calibration is summarized in Table (4.5).

4.7 DAQ PID Performance

Both threshold CO₂ Cherenkov detector and a double-layered lead glass detector provide particle identification (PID). The PID performance is characterized by four variables: η_C^e electron detection efficiency in the gas Cherenkov detector, η_{LG}^e electron detection efficiency in the lead glass detector, r_C^π pion rejection factor in gas Cherenkov detector and r_{LG}^π pion rejection factor in the lead glass detector. The PID performance of the DAQ system was studied with calibration runs taken at low beam currents using fbTDC signals along with the ADC data of all detector signals recorded by the standard DAQ. The general approach to study PID performance is to study the fraction of electrons (pions) identified by the detectors from a clean electron (pion) sample. Since the particle identification mechanism of the Cherenkov detector and lead glass detector are different, the PID performance of these two detectors are

HRS	LHRS					RHRS	
Kinematics	DIS#1	RES#7	DIS#2	RES#3	RES#4	DIS#2	RES#5
$\theta(^{\circ})$	12.9	15.0	20	12.9	12.9	20	12.9
$E_b(GeV)$	6.0674	6.0674	6.0674	4.8674	4.8674	4.8674	4.8674
$E'(GeV)$	3.66	3.66	2.63	4.0a	3.66	2.63	3.1
HRS survey	Y	N	Y	N	N	Y	N
$\delta D(\text{survey})(\text{mm})$	0.5		0.5			0.5	
Carbon multi foil data	Y	N	Y	Y	Y	Y	Y
				0.5	0.5	0.5	0.5
$\delta D(\text{from data})(\text{mm})$							
$\delta D(\text{no survey},$ $\text{no data})(\text{mm})$		5					
δ_{zreact} , calibration accuracy (mm)	0.3	N/A	0.4	2.0	0.3	0.7	1.1
δ_{zreact} actual foil position	2.5	N/A	2.5	2.5	2.5	2.5	2.5
$\Delta\theta$ from vertex calibration	0.672	4.464	0.893	0.779	0.672	0.901	0.704
sieve survey	N	N	N	N	N	N	N
sieve data	N	N	N	Y	Y	N	N
Δx_{sieve} , from prior survey (mm)	0.51	0.51	0.51	0.51	0.51	0.51	0.51
Δx_{sieve} , calibration accuracy (mm)	0.1	N/A	0.1	0.1	0.1	0.1	0.1
extra $\Delta\phi_{tg}$ (mrad)	0.5	0.5	0.5			0.5	0.5
$\Delta\theta$ from angle calibration	0.682	0.676	0.682	0.464	0.464	0.676	0.676
Total $\Delta\theta$ (mrad)	0.957	4.515	1.124	0.907	0.816	1.134	0.976
Total $\Delta\theta/\theta$ (%)	0.425	1.725	0.322	0.403	0.363	0.325	0.434
$\Delta E'/E'$	5×10^{-4}						
Total $\Delta Q^2/Q^2$ (%)	0.850	3.449	0.644	0.805	0.725	0.650	0.867

Table 4.5: PVDIS Q^2 uncertainty due to optics calibration for each HRS. The kinematics are ordered from left to right in the chronological order.

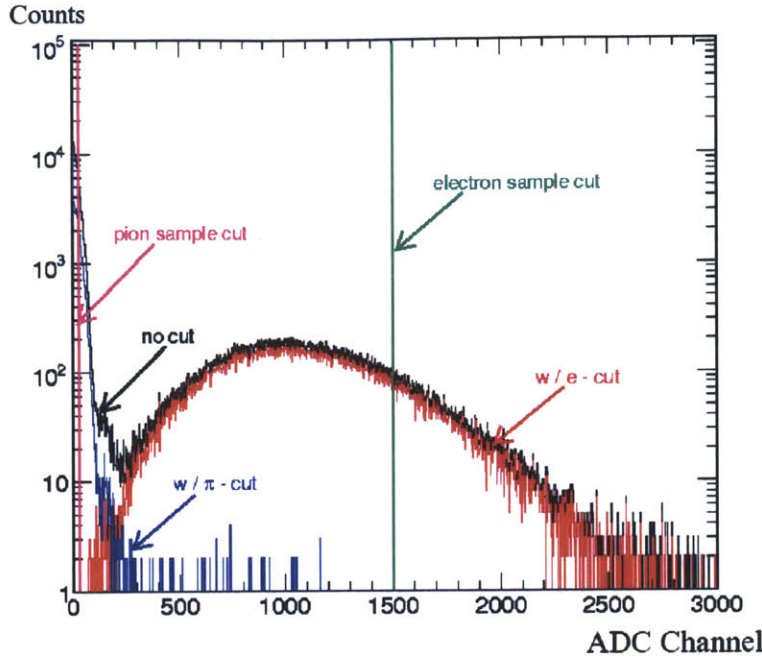


Figure 4-9: An ADC signal of the right HRS gas Cherenkov detector without a cut (black), after lead glass detector's electron cut (red) and pion cut (blue). The vertical green line shows a cut $ADC > 1500$ for selecting electrons, and the vertical magenta line shows a cut $ADC < 30$ for selecting pions.

independent. Therefore, clean electron and pion samples can be selected from lead glass detector to study the PID performance of gas Cherenkov detector and vice versa for lead glass detector.

Fig. (4-9) shows a spectrum of an ADC signal from the right HRS gas Cherenkov detector both before and after the lead glass detector electron and pion cuts. The spectrum from the left HRS is similar. As shown in the plot, electrons and pions have different distributions. In order to perform a precise PID efficiency analysis, we need to apply a very tight cut so that the selected sample of electrons and pions have the least contamination. As can be seen, a clean electron sample can be selected at $ADC > 1500$ as indicated by the vertical green line, and a clean pion sample can be selected at $ADC < 10$ as indicated by the vertical magenta line.

When passing through the double-layered lead glass detector, electrons generate significantly more Cherenkov light in both the first and second layer than pions due to electromagnetic showers. Therefore, the energy distribution of electrons and pions are different in a 2-dimensional (2D) Preshower-Shower ADC plot. Thus, one can

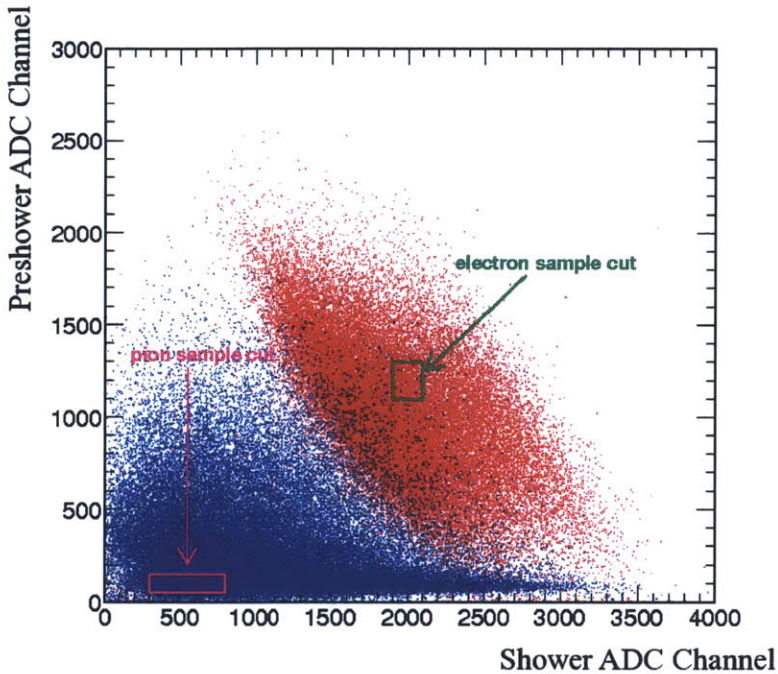


Figure 4-10: Two-dimensional distribution of signals strength in Preshower and Shower lead glass detector, after the gas Cherenkov ADC electron cut (red) and the pion cut (blue). The green box shows a cut for selecting clean electron sample, and the magenta box shows a cut for selecting clean pion sample.

separate pions from electrons, and vice versa, by applying a 2-dimensional cut in the energy deposition. Fig. (4-10) shows the 2D distribution of the energy depositions in the preshower and shower detectors before and after Cherenkov electron (red) and pion (blue) cuts. As can be seen, a clean electron sample can be chosen as events located in the green box, while the magenta box gives a clean pion sample.

Events that triggered the DAQ form a timing peak in the corresponding fbTDC spectrum of the standard DAQ as shown in Fig. (4-11). A cut on this peak was used to select those events (electrons) identified by the DAQ system. Fig. (4-12) shows the Preshower vs. Shower signals for group 2 on the Left HRS. A comparison between no fbTDC cut and with a cut on the fbTDC signal of the electron wide trigger from this group clearly shows the hardware cuts on the preshower and the total shower signals which indicates that the DAQ is selecting the correct events as electrons. The cuts could be adjusted by changing the discriminator thresholds.

Low-rate calibration data were taken daily during the experiment to monitor the DAQ PID performance, and corrections were applied to the asymmetry data.

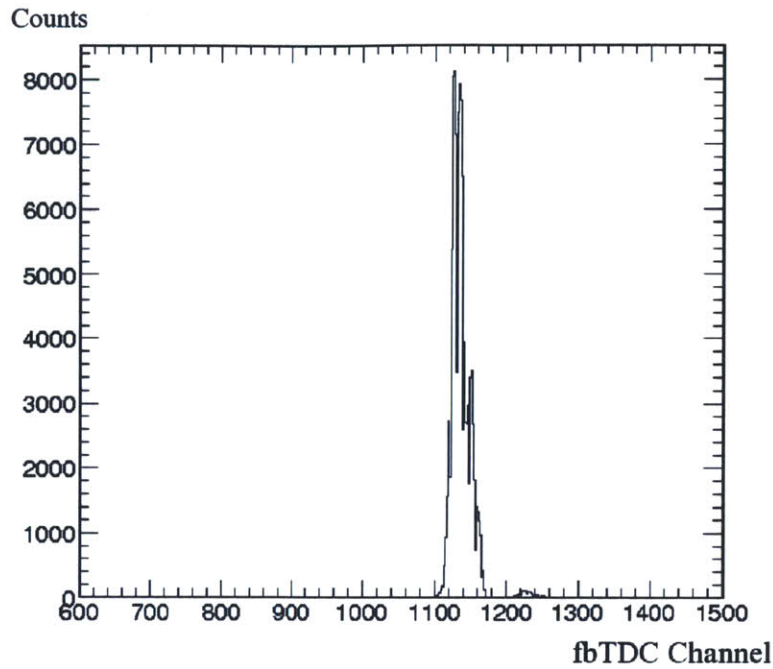


Figure 4-11: fbTDC signal of electron global counter.

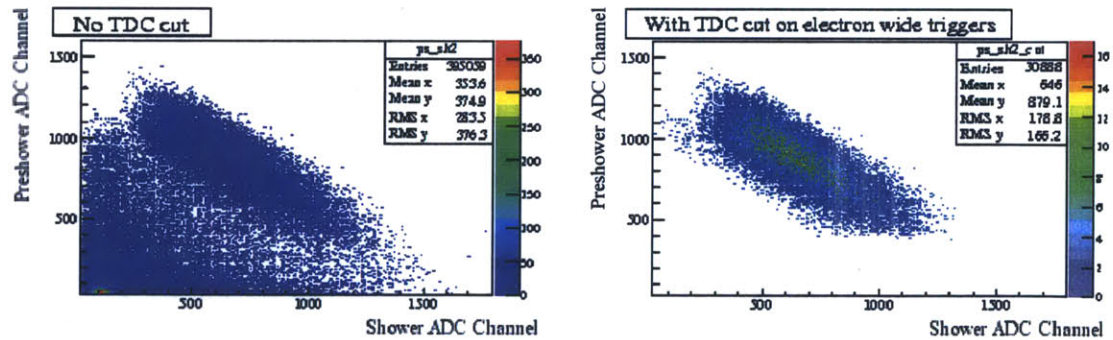


Figure 4-12: Preshower vs. Shower ADC spectrum (sum of 8 blocks each) for group 2 of the Left HRS without a fbTDC cut (left) and with cut on the group 2 electron wide trigger fbTDC signal (right). The events near the vertical axis, around ADC channels (200,1000), are electrons that deposited energy in overlapping blocks between group 2 and group 1 (or group 3) and are recorded by the other group.

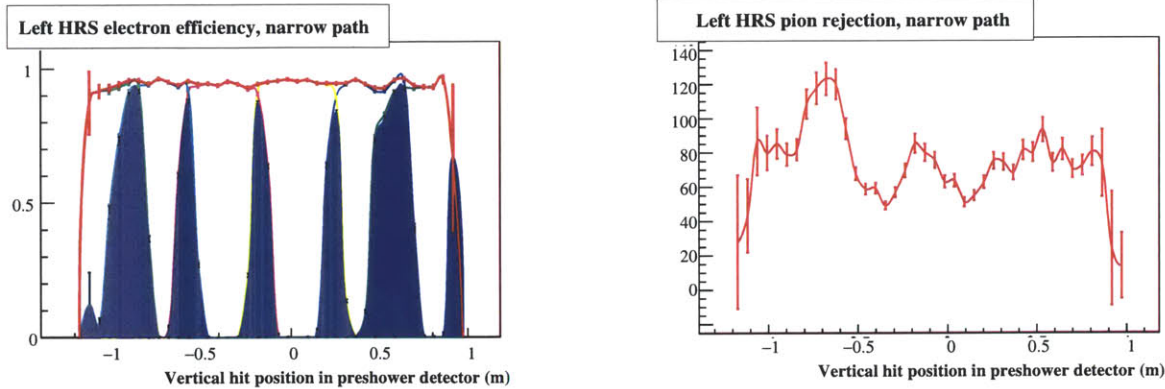


Figure 4-13: Electron detection efficiency (left) and pion rejection factor (right) vs. vertical (dispersive) hit position of particles in the preshower detector for the narrow electron triggers in the Left HRS. For electron efficiencies, the total efficiency is shown by the red curve, while blue shaded area indicates events that are recorded by the two adjacent groups. The error bars are statistical only. PID performance for the wide path and the Right HRS are similar.

Not only the overall PID performance of whole spectrometer, but also variations in the electron efficiency and pion rejection factor across the spectrometer acceptance were studied as they affect the Q^2 measurement across the spectrometer acceptance. Electron efficiency and pion rejection factors of the lead-glass detectors of the Left HRS during a one-hour run are shown in Fig. (4-13) as functions of the location of particles in the preshower detector. An averaged 95% electron efficiency and 100 pion rejection factor of the lead-glass detector were achieved in the Left HRS. The PID performance in the Right HRS was similar.

The gas Cherenkov detectors signals were read out by 10 PMTs on each HRS. Signals from all 10 PMTs were summed in an analog-sum module and sent to a discriminator. The discriminator output was sent to the DAQ (as shown in Fig. (3-2)) as well as fbTDCs. Fig. (4-14) and Fig. (4-10) show the Cherenkov ADC sum and 2D lead glass spectrum respectively with and without the fbTDC cut. They clearly demonstrate the capability of selecting electrons while rejecting pions.

Pion contamination in the electron trigger affects the measured electron asymmetry. Assuming a fraction $f_{\pi/e}$ of π^- contaminates into the electron triggers and the pure electron fraction is $1 - f_{\pi/e}$, the measured asymmetry is then

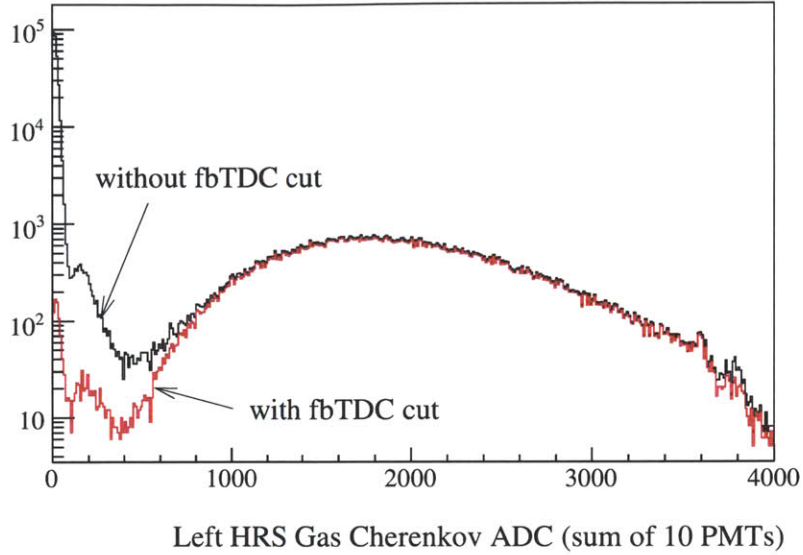


Figure 4-14: Gas Cherenkov ADC data (sum of 10 PMTs) for the Left HRS with a fbTDC cut on the Cherenkov discriminator output (red) and without (black).

$$A_m = f_{\pi/e} A_\pi + (1 - f_{\pi/e}) A_e \quad (4.15)$$

where A_e is the true electron asymmetry and A_π is the pion asymmetry. The pion contamination in the electron trigger, $f_{\pi/e}$, comes from two effects:

1. There is a possibility that a pion could trigger both the lead-glass and the gas Cherenkov detectors and is misidentified as electron. This possibility is determined by the overall pion rejection capability of the whole DAQ system, which is a direct combination of the pion rejection factors of the two detectors and is below 10^{-4} .
2. The width of the electron VETO signal: Electrons opened VETO gate for 150ns. Thus, electron VETO gate lost pion rejection capability for pions that arrived later than electrons but before the closing of the electron VETO gate, causing misidentification of pions as electron triggers. $R_e \eta_e^{GC}[150\text{ns} - \tau_{dt,n(w)}]$ is the probability for a pion to arrive within a valid electron VETO signal and thus can not be rejected by the lead-glass detectors.

The sum of the two effects can be written as

$$f_{\pi/e,n(w)} = \frac{R_\pi / (r_\pi^{GC} r_\pi^{LG})}{R_e \eta_e^{GC} \eta_e^{LG}} + \frac{(R_\pi / r_\pi^{LG}) (R_e \eta_e^{GC} [150ns - \tau_{dt,n(w)}])}{R_e \eta_e^{GC} \eta_e^{LG}}, \quad (4.16)$$

where R_e and R_π are the electron and pion raw rate, respectively, and r_π^{LG} , r_π^{GC} are pion rejection of lead glass and gas Cherenkov detector, η_e^{LG} , η_e^{GC} are electron efficiency of lead glass and gas Cherenkov and $\tau_{dt,n(w)}$ is the DAQ group dead time of the lead glass detector in narrow (wide) path, which is presented in the next section.

The electron detection efficiency and pion rejection factor averaged throughout the experiment are shown in Table (4.6) for different kinematics and for the Left and the Right HRS separately. Also shown are the π/e rate ratio obtained from the data and the resulting pion contamination $f_{\pi/e}$ evaluated separately for the narrow and the wide paths.

As shown in Table (4.6), the overall pion contamination was on the order of 2×10^{-4} or lower. The uncertainty in the electron asymmetry due to pion contamination is therefore on the order of 2×10^{-4} and is negligible compared to the 3-4% statistical uncertainty.

In order to quantify how pion background affected the electron asymmetry, it is important to extract the pion asymmetries from pion triggers. Hence, a complete PID analysis was carried out on the pion triggers of the DAQ. The electron contamination in the pion trigger $f_{e/\pi}$ was evaluated in a similar manner as $f_{\pi/e}$ above, as following

$$f_{e/\pi} = \frac{R_e / (r_e^{GC} r_e^{LG})}{R_\pi \eta_\pi^{GC} \eta_\pi^{LG}} + \frac{(R_e / r_e^{LG}) (R_\pi \eta_\pi^{GC} [150ns - \tau_{dt}])}{R_\pi \eta_\pi^{GC} \eta_\pi^{LG}} \quad (4.17)$$

Results for electron contamination in the pion trigger is summarized in Table (4.7).

Kinematics and Spectrometer combinations			
	Q2 = 1.1 (GeV/c)2	Q2 = 1.9 (GeV/c)2	
HRS	Left	Left	Right
Electron detection efficiency η_e			
GC	(99.14 \pm 0.02)%	(99.03 \pm 0.03)%	(98.19 \pm 0.06)%
LG, narrow	(91.93 \pm 0.04)%	(94.50 \pm 0.06)%	(94.36 \pm 0.04)%
LG, wide	(92.88 \pm 0.04)%	(95.79 \pm 0.06)%	(95.23 \pm 0.04)%
combined, narrow	(91.14 \pm 0.04)%	(93.58 \pm 0.06)%	(92.65 \pm 0.07)%
combined, wide	(92.08 \pm 0.04)%	(94.86 \pm 0.06)%	(93.51 \pm 0.07)%
Pion rejection r_π			
GC	(158.6 \pm 3.5) : 1	(301.2 \pm 5.2) : 1	(414.3 \pm 6.2) : 1
LG, narrow	(101.5 \pm 1.6) : 1	(78.9 \pm 0.9) : 1	(72.7 \pm 0.3) : 1
LG, wide	(103.9 \pm 1.7) : 1	(81.5 \pm 1.0) : 1	(74.3 \pm 0.3) : 1
Pion contamination in the electron trigger $f_{\pi/e}$, narrow path			
actual rate R_π/R_e	0.7	3.5	3.5
$f_{\pi/e,n}$	1.61×10^{-4}	2.20×10^{-4}	1.99×10^{-4}
$\Delta f_{\pi/e,n}$ (stat.)	$\pm 3.34 \times 10^{-6}$	$\pm 4.62 \times 10^{-6}$	$\pm 2.15 \times 10^{-6}$
$\Delta f_{\pi/e,n}$ (syst..)	$\pm 2.01 \times 10^{-5}$	$\pm 2.29 \times 10^{-5}$	$\pm 2.08 \times 10^{-5}$
$\Delta f_{\pi/e,n}$ (var.)	$\pm 9.76 \times 10^{-6}$	$\pm 1.71 \times 10^{-5}$	$\pm 1.15 \times 10^{-5}$
$\Delta f_{\pi/e,n}$ (total)	$\pm 2.21 \times 10^{-5}$	$\pm 2.86 \times 10^{-5}$	$\pm 2.38 \times 10^{-5}$
Pion contamination in the electron trigger $f_{\pi/e}$, wide path			
$f_{\pi/e,w}$	1.00×10^{-4}	1.83×10^{-4}	1.59×10^{-4}
$\Delta f_{\pi/e,w}$ (stat.)	$\pm 2.28 \times 10^{-6}$	$\pm 4.72 \times 10^{-6}$	$\pm 2.10 \times 10^{-6}$
$\Delta f_{\pi/e,w}$ (syst..)	$\pm 1.71 \times 10^{-5}$	$\pm 2.01 \times 10^{-5}$	$\pm 1.96 \times 10^{-5}$
$\Delta f_{\pi/e,w}$ (var.)	$\pm 9.81 \times 10^{-6}$	$\pm 1.51 \times 10^{-5}$	$\pm 1.02 \times 10^{-5}$
$\Delta f_{\pi/e,w}$ (total)	$\pm 1.97 \times 10^{-5}$	$\pm 2.52 \times 10^{-5}$	$\pm 2.21 \times 10^{-5}$

Table 4.6: Average electron detection efficiencies and pion rejection factors achieved through the lead glass (LG), the gas Cherenkov (GC) detectors and the combined performance. The error bars of the efficiency and the rejection factors are statistical only. The error bars for $f_{\pi/e}$ are shown separately for statistical uncertainties, systematic uncertainties due to our understanding of the rates, detector efficiencies and deadtimes, and systematic uncertainties due to day-to-day variations.

Kinematics and Spectrometer combinations			
	Q2 = 1.1 (GeV/c)2	Q2 = 1.9 (GeV/c)2	
HRS	Left	Left	Right
Pion detection efficiency η_π			
GC	(99.52 ± 0.01)%	(99.73 ± 0.01)%	(99.74 ± 0.01)%
LG, narrow	(21.67 ± 0.01)%	(79.72 ± 0.02)%	(15.61 ± 0.01)%
LG, wide	(21.67 ± 0.01)%	(79.71 ± 0.02)%	(15.60 ± 0.01)%
combined, narrow	(21.57 ± 0.01)%	(79.70 ± 0.02)%	(15.57 ± 0.01)%
combined, wide	(21.57 ± 0.01)%	(79.69 ± 0.02)%	(15.56 ± 0.01)%
Electron rejection r_e			
GC	(31.42 ± 0.78) : 1	(89.44 ± 2.48) : 1	(48.48 ± 1.55) : 1
LG, narrow	(1.0468 ± 0.0003) : 1	(1.0487 ± 0.0005) : 1	(1.0271 ± 0.0002) : 1
LG, wide	(1.0469 ± 0.0003) : 1	(1.0499 ± 0.0005) : 1	(1.0279 ± 0.0002) : 1
Electron contamination in the pion trigger $f_{e/\pi}$, narrow path			
actual rate R_π/R_e	0.7	3.5	3.5
$f_{e/\pi,n}$	0.2738	0.03197	0.00967
$\Delta f_{e/\pi,n}$ (stat.)	± 0.00386	± 0.00080	0.00026
$\Delta f_{e/\pi,n}$ (syst..)	± 0.01382	± 0.00143	0.00026
$\Delta f_{e/\pi,n}$ (var.)	± 0.05441	± 0.00303	0.00112
$\Delta f_{e/\pi,n}$ (total)	± 0.05613	± 0.00335	0.00115
Electron contamination in the pion trigger $f_{e/\pi}$, wide path			
$f_{e/\pi,w}$	0.2246	0.02672	0.00854
$\Delta f_{e/\pi,w}$ (stat.)	± 0.00386	± 0.00079	0.00026
$\Delta f_{e/\pi,w}$ (syst..)	± 0.01236	± 0.00127	0.00062
$\Delta f_{e/\pi,w}$ (var.)	± 0.05255	± 0.00308	0.00109
$\Delta f_{e/\pi,w}$ (total)	± 0.05399	± 0.00333	0.00125

Table 4.7: Average pion detection efficiencies and electron rejection factors achieved through the lead glass (LG), the gas Cherenkov (GC) detectors, and the combined performance. The error bars of the efficiencies and the rejection factors are statistical only. The error bars for $f_{e/\pi}$ are shown separately for statistical uncertainties, systematic uncertainties, and the systematic uncertainty due to day-to-day variations.

4.8 DAQ Deadtime

4.8.1 Deadtime Overview

Deadtime is the amount of time after an event during which the system is unable to record another event. Identifying the exact value of the deadtime is always a challenge in counting experiments. Assuming deadtime is τ and event rate is R , the probability of an event falling in the time window τ after a previous event, is $1 - e^{-R\tau}$. Such events are lost due to the deadtime. Therefore, the actual measured rate R_m is

$$R_m = R(1 - (1 - e^{-R\tau})) = Re^{-R\tau} \quad (4.18)$$

In the limit of $R\tau \ll 1$, Eq. (4.18) can be approximated as

$$R_m \approx R(1 - R\tau) \quad (4.19)$$

Different helicity states can have different rates. Hence the rates for two helicity states + and - is

$$R_m^\pm \approx R^\pm(1 - R^\pm\tau). \quad (4.20)$$

Therefore, this deadtime effect cannot be canceled out in the asymmetry calculation, and the correction due to the deadtime effect is

$$A_m = \frac{R_m^+ - R_m^-}{R_m^+ + R_m^-} \approx A(1 - R\tau) = A(1 - \delta), \quad (4.21)$$

where A_m and A are the measured and true asymmetries respectively. It is observed that the deadtime δ contributes to the asymmetry at first order, and hence it is an important systematic effect that needs to be thoroughly understood. During the experiment, δ was on the order of (1-2)%. Since the statistical accuracy on the asymmetry is (3-4)%, it was sufficient to know δ with a (10-20)% relative accuracy so that it would become a negligible systematic error.

The total DAQ deadime consists of three sources as listed below:

1. The “group” deadtime: the preshower and shower PMT signals generate deadtime when passing through discriminators and logic AND modules.
2. The “veto” deadtime: Scintillator and Cherenkov signals are combined to form the VETO signal, which is served as the “gate” to accept group triggers. Any loss of veto signal due to the deadtime would cause a failure in recording the group trigger.
3. The “OR” deadtime: deadtime due to the logical OR module used to combine all group triggers into the final global triggers.

In order to evaluate the DAQ deadtime, a full-scale trigger simulation was performed. This trigger simulation is described in the next section followed by results of the group, veto, and OR deadtimes as well as of the total deadtime correction that was applied to the asymmetry data.

4.8.2 Trigger Simulation

A full-scale trigger simulation software, named “The Hall A Trigger Simulation” (HATS), was developed for the purpose of studying the deadtime in this experiment. The simulation took inputs from the detectors, simulated the functioning of the DAQ system and provided detailed analysis of the DAQ’s deadtime effect.

The inputs to HATS included:

- A full DAQ map
- Event rates from the gas Cherenkov, scintillators, and lead glass detectors
- The shape of analog signals from the lead glass, which was modeled by the function

$$S(t) = Ate^{-t/\tau}, \quad (4.22)$$

where A is related to the amplitude of the signal, and τ is the time constant characterizing the shape of the lead glass analog signal. As smaller τ gives a

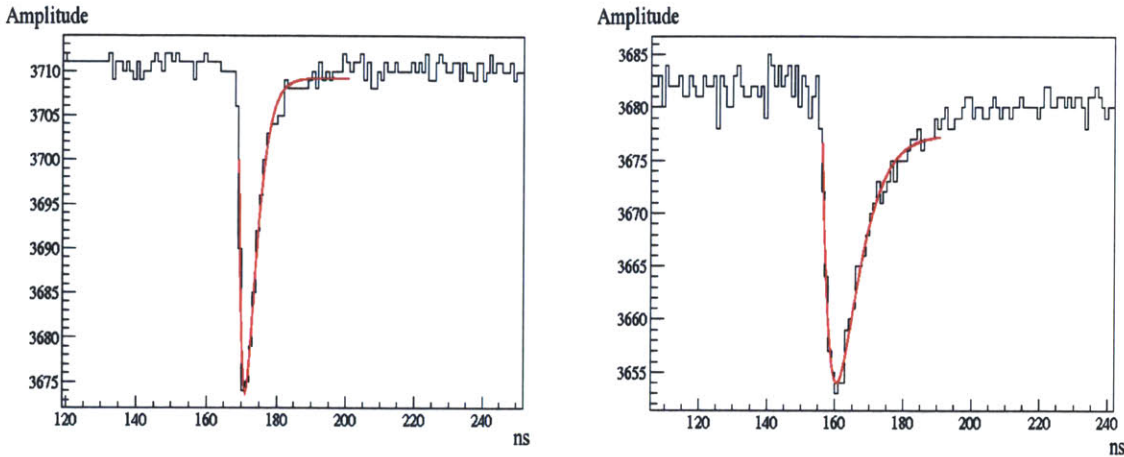


Figure 4-15: Calibration of time constant τ for Preshower (left) and Shower (right) of the Right HRS. The FADC snapshot (black) is compared with the fit $S(t) = Ate^{-t/\tau}$ (red).

faster rise time. Both A and τ were calibrated by using FADC data from real signals as shown in Fig. (4-15).

In HATS the DAQ system was first built on the software level according to the DAQ map. Then the input of physical signals were generated randomly according to the event rates and calibrated signal shapes. With sufficient input provided, HATS was able to simulate signals from all discriminators, AND, and OR modules. Fig. (4-16) shows a part of the DAQ electronics and the simulated results for a very short time period. By comparing output to input signals, HATS reproduced the fractional loss due to deadtime.

4.8.3 Group Deadtime Measurement

In order to study the group deadtime, a “tagger”, which was a fixed-frequency logic pulser signal generated using gate generators, was mixed with real physics signals (preshower and shower PMT signals) and fed into the DAQ during data taking, see Fig. (3-2) and Fig. (4-17). In this way, the tagger passes through the exact same set of electronics as the physics signals do, and thus should “see” the same deadtime. This tagger scheme was applied to every individual group. At the end of each group,

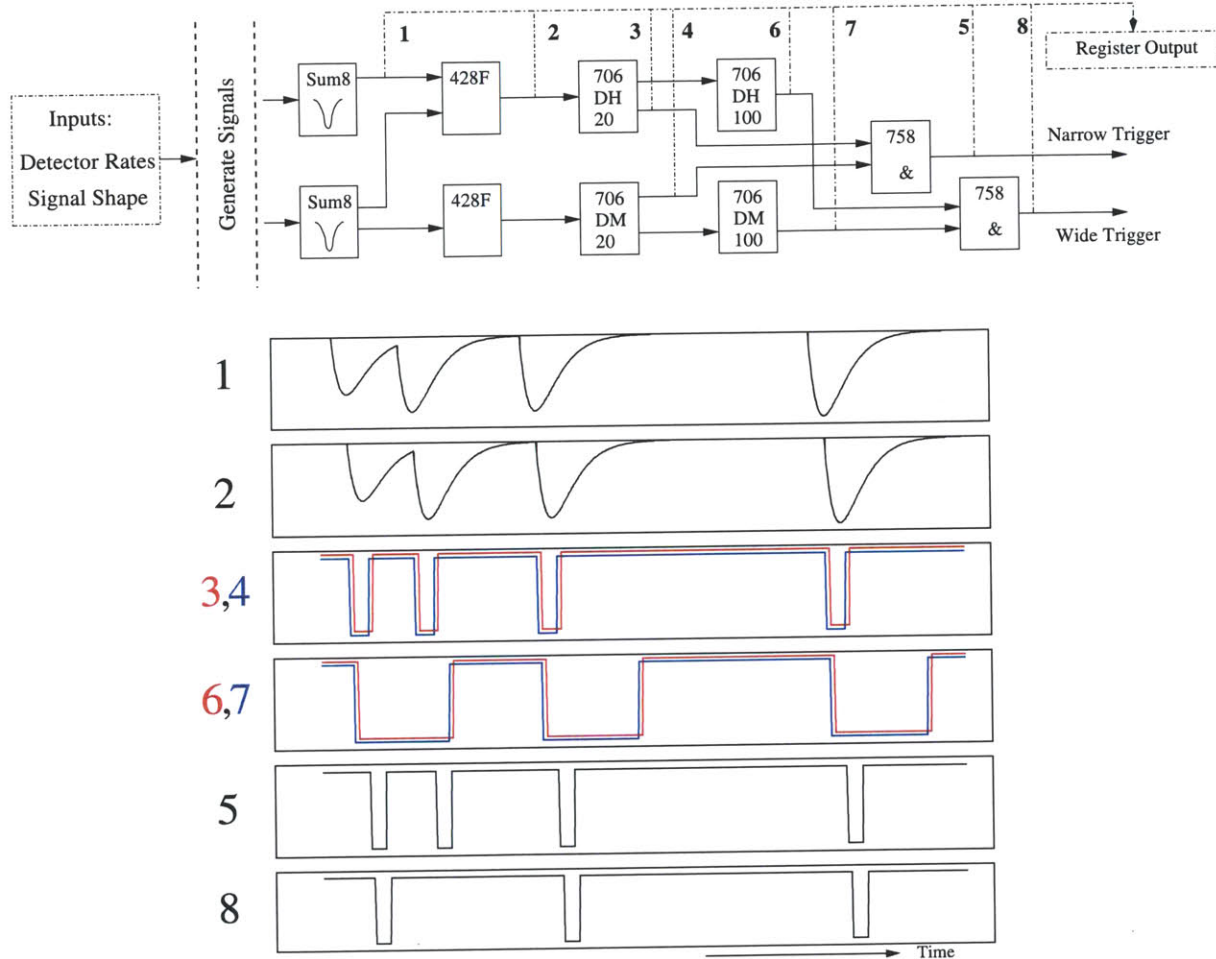


Figure 4-16: Top: A part of the group electron trigger. The numbers correspond to:
 1 - Shower sum of the group; 2 - Total shower sum of the group; 3 - Total shower discriminator output (high threshold), narrow path; 4 - Preshower discriminator output (medium threshold), narrow path; 5 - group electron trigger, narrow path; 6 - Total shower discriminator output, wide path; 7 - Preshower discriminator output, wide path; 8 - group electron trigger, wide path.
 Bottom: Signals 1-8 as simulated by HATS. Note that the second physical event is recorded by the narrow path group trigger (5) but not the wide path (8) due to deadtime loss.

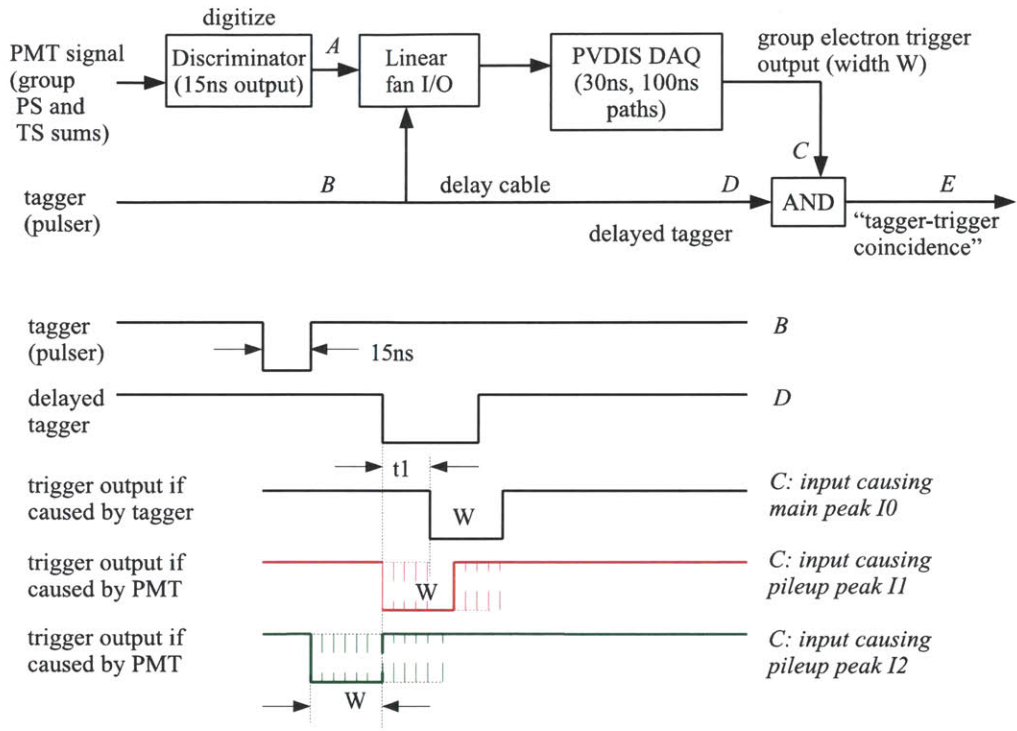


Figure 4-17: schematic diagram of the tagger setup and signal timing sequence.

we pick out the tagger from the mixing signals by requiring a coincidence between the group electron trigger and the tagger delayed by the DAQ's response time. If there is no physics signal, every tagger produces an electron trigger and then a coincidence signal, thus the output coincidence rate R_o is exactly the same as the input tagger rate R_i . However, with the presence of high-rate physics signals, which are random with respect to the tagger pulses, a fraction of the tagger pulses are blocked by their closely preceding physics signals due to deadtime. The difference between R_o and R_i provided a direct measurement of the group deadtime.

The deadtime measured for the wide path was approximately 100 ns which is the width of the electron discriminator trigger in the wide path as expected. For the narrow path, although the discriminator's width was set to be 30ns, the deadtime was dominated by the lead glass PMT signal, which was around 60~70 ns instead of the width of the discriminator output. This observation was also confirmed by FADC snapshots and is in agreement with both tagger data and simulation.

4.8.4 VETO Deadtime Measurement

Although the deadtime loss of each group was measured using the tagger signals, the dominating term in the total deadtime was from the veto electronics because the trigger rate from scintillators and the gas Cherenkov was much higher than the individual lead-glass group rates. As simulation of the veto deadtime was compared with FADC data and the agreement was found to be at the 20% level or better. This corresponds to a contribution to the uncertainty of deadtime of less than 0.2%.

4.8.5 “OR” Deadtime Measurement

After subtracting the group and veto deadtimes from the total simulated deadtime, the remaining was attributed to the logical OR module. There was no direct measurement of the logical OR deadtime, but its fractional contribution can be calculated as one minus those from group and veto, and its uncertainty is estimated from the difference between the simulation and the analytical results. The result is shown in Table (4.8).

4.8.6 Total Deadtime Evaluation

The simulated deadtime loss of the global electron triggers and its decomposition into group, veto, and OR are shown in Table (4.8). The deadtime corrections at an $100 \mu\text{A}$ beam current for the narrow path triggers are $(1.45 \pm 0.13)\%$ and $(0.89 \pm 0.20)\%$, and for the wide path triggers are $(1.64 \pm 0.16)\%$ and $(0.93 \pm 0.22)\%$, for $Q^2=1.1$ and $1.9 (\text{GeV}/c)^2$, respectively. These are direct corrections to the measured asymmetries and the uncertainties are small compared to other dominant systematic uncertainties such as that of the beam polarization.

4.9 Asymmetry Measurement

The physics asymmetries measured in this experiment were predicted to be 91 and 160 ppm for $Q^2 = 1.1$ and $1.9 (\text{GeV}/c)^2$, respectively. The measured asymmetries

HRS, Q^2 (GeV/c^2)	Path	fractional contribution			Total deadtime loss at 100 μA
		Group	Veto	OR	
Left, 1.1	n	(20.6 \pm 2.1)%	(51.3 \pm 4.5)%	(28.1 \pm 4.7)%	(1.45 \pm 0.10)%
	w	(29.5 \pm 2.4)%	(45.3 \pm 4.0)%	(25.3 \pm 4.6)%	(1.64 \pm 0.11)%
Left, 1.9	n	(5.42 \pm 0.8)%	(81.1 \pm 7.1)%	(13.5 \pm 7.0)%	(0.50 \pm 0.05)%
	w	(8.39 \pm 0.4)%	(77.3 \pm 6.8)%	(14.3 \pm 8.0)%	(0.52 \pm 0.06)%
Right, 1.9	n	(2.9 \pm 0.2)%	(80.6 \pm 18.5)%	(16.5 \pm 12.7)%	(0.89 \pm 0.20)%
	w	(4.3 \pm 0.4)%	(76.6 \pm 17.5)%	(19.1 \pm 15.5)%	(0.93 \pm 0.22)%

Table 4.8: Simulated DAQ deadtime loss in percent for all kinematics and for both narrow (n) and wide (w) paths, along with the fractional contributions from the group, veto, and OR deadtimes. The uncertainty of the total deadtime is from the uncertainties of the group, veto and OR added in quadrature.

were formed from counting events of each beam helicity pair with 33-ms of helicity right and 33-ms of helicity left beam, which were normalized by the beam charge. Two independent asymmetry analyses were carried out. To avoid bias in the analysis, the electron asymmetries from DIS kinematics were blinded by adding a constant blinding factor during the analysis. The statistical uncertainties of the PVDIS asymmetry were 3% and 4% for $Q^2 = 1.1$ and 1.9 (GeV/c^2), respectively. Currently, the DIS electron asymmetries from the two independent analysis agree within 0.2 ppm, about 1/20 of the statistical uncertainty. The statistical quality of the measured asymmetries is shown in Fig. (4-18). The non-Gaussian tail for DIS#1 ($Q^2 = 1.1$ (GeV/c^2)) taken on the left HRS and for DIS#2 ($Q^2 = 1.9$ (GeV/c^2)) taken on the right HRS are due to variations in the beam current (70-105 μA) used at the beginning of the experiment. This non-Gaussian tail is not present in later data, where a constant 105 μA current was used, as can be seen from data on DIS#2 collected from the left HRS in the second plot of Fig. (4-18). Fig. (4-19) shows the pull distribution of pair-wise asymmetries taken during constant high beam current (100~105 μA). Here, “pull” is defined as

$$p_i \equiv (A_i - \langle A \rangle) / \delta A_i \quad (4.23)$$

where A_i is the asymmetry extracted from the i-th beam helicity pair, $\delta A_i = 1/\sqrt{N_i^R + N_i^L}$ its statistical uncertainty with $N_i^{R(L)}$ the event count from the right (left) helicity

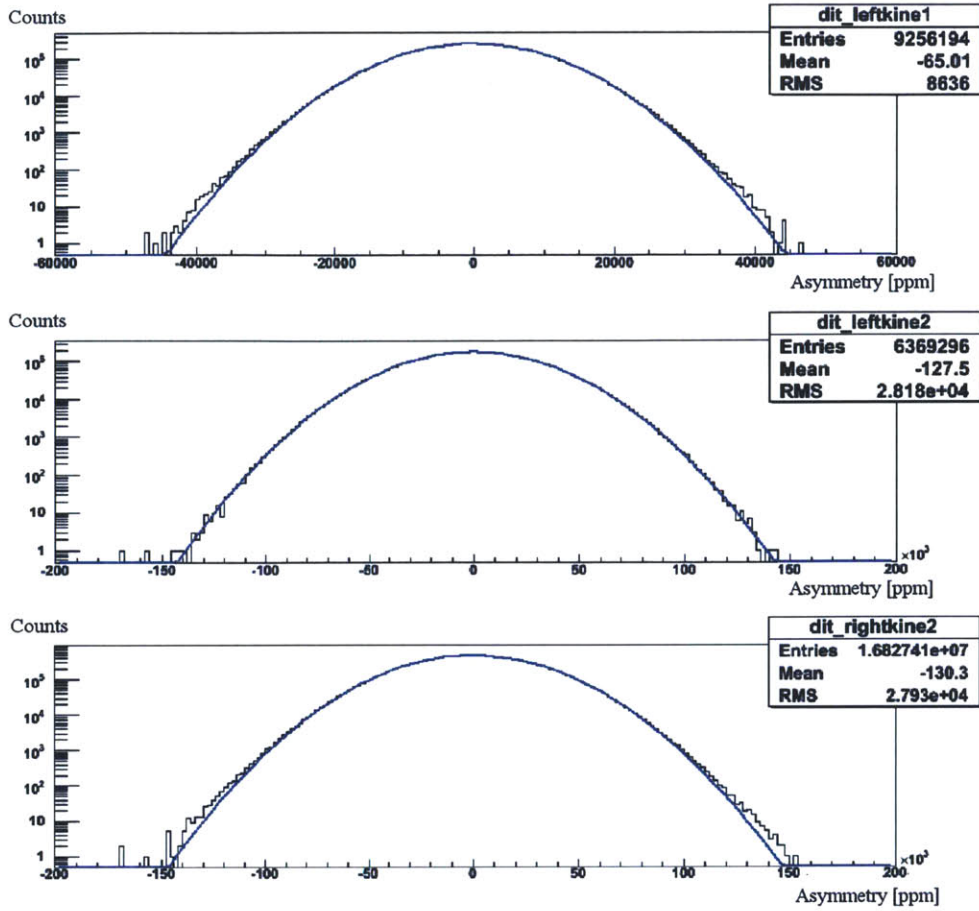


Figure 4-18: Overall statistical quality of the data after the dithering correction. From top to bottom: DIS#1 taken on the left HRS, DIS#2 taken on the left HRS, and DIS#2 taken on the right HRS. All asymmetries shown here are blinded.

pulse of the pair, and $\langle A \rangle$ is the asymmetry averaged over all beam pairs. One can see that the asymmetry spectrum agrees to five orders of magnitude with the Gaussian distribution as expected from purely statistical fluctuations.

The preliminary asymmetries after beam polarization, PID efficiency, pion dilution, and deadtime corrections are presented in Table (4.9). The corrected asymmetry for DIS#1 is $A_d = 90.99 \pm 3.15(\text{stat}) \pm 2.73(\text{syst})$ ppm and for DIS#2 after combination of DIS#2 (Left) and DIS#2 (right) is $A_d = 160.62 \pm 6.48(\text{stat}) \pm 2.99(\text{syst})$ ppm, in agreement with predictions. The statistical uncertainties of the PVDIS asymmetries are 3% for DIS#1 at $Q^2 = 1.1$ $(\text{GeV}/c)^2$ and 4% for DIS#2 at $Q^2 = 1.9$ $(\text{GeV}/c)^2$, respectively, which fulfill the goal of this experiment.

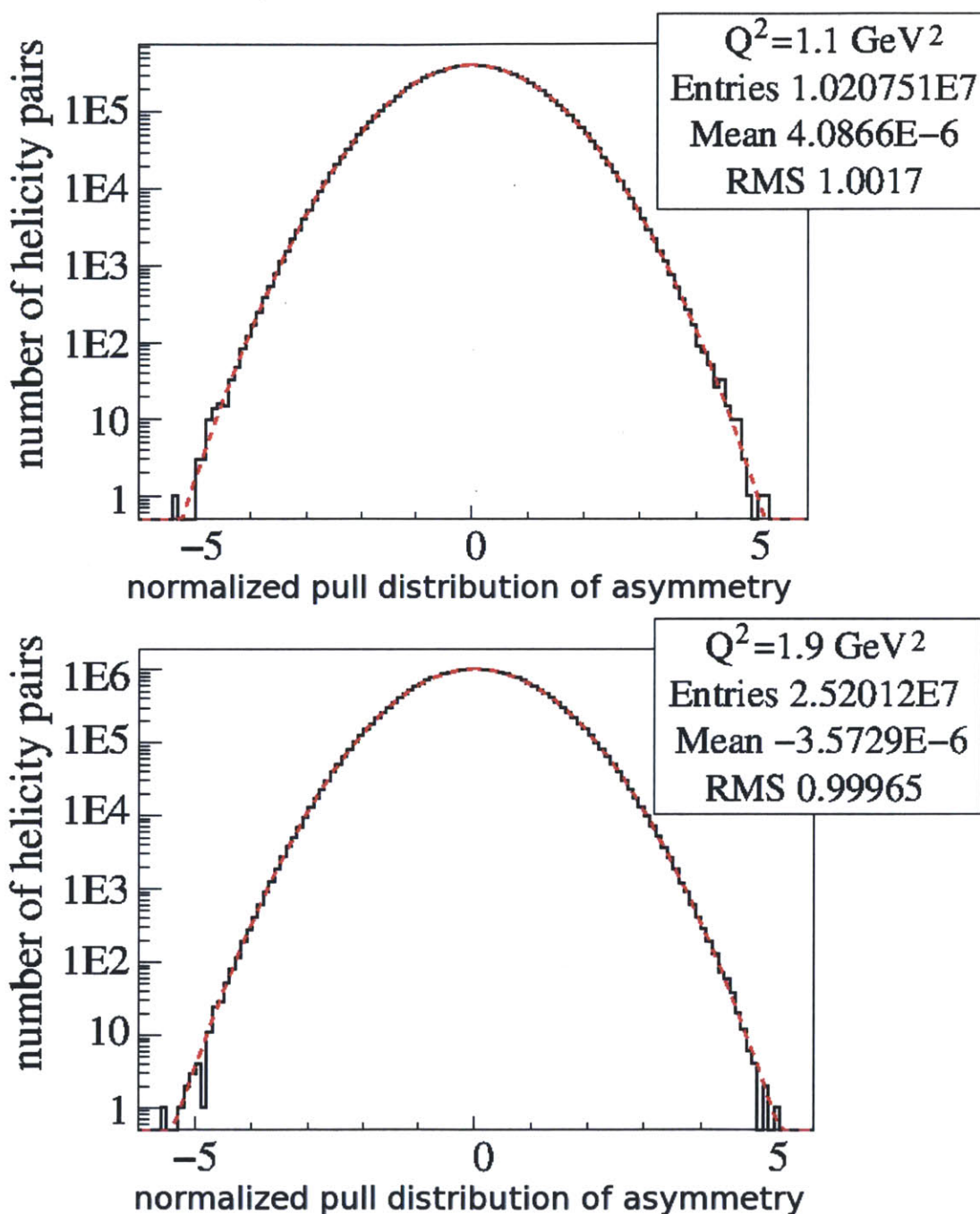


Figure 4-19: Pull distribution of the asymmetry for the global electron narrow trigger for $Q^2=1.1$ (GeV/c) 2 (top) and 1.9 (GeV/c) 2 (bottom), respectively.

Kinematics	DIS#1(Left)	DIS#2(Left)	DIS#2(Right)
Raw Asymmetry A_d (ppm)	-78.44	-140.49	-140.57
Beam Polarization	13.4%	12.0%	12.7%
Deadtime correction	1.49%	0.84%	0.86%
PID efficiency	0.048%	0.091%	0.161%
Q^2	0.725%	0.575%	0.640%
Pion Dilution	0.019%	0.025%	0.024%
Corrected Asymmetry A_c (ppm)	90.99	159.21	161.10
Statistical Error (ppm)	3.15	12.08	7.67
Systematics Error (ppm)	2.73	2.61	3.16

Table 4.9: Preliminary asymmetries and corrections.

Chapter 5

Summary and Proposed Future Work

An experiment that measured the parity violating (PV) asymmetry A_d in $e^-{}^2\text{H}$ deep inelastic scattering at $Q^2 \approx 1.1$ and 1.9 (GeV/c) 2 was completed at the Thomas Jefferson National Accelerator Facility in experimental Hall A. A scaler-based counting DAQ with hardware-based particle identification was successfully implemented. The pion contamination in the electron samples was controlled to a level of 2×10^{-4} or lower with an electron detection efficiency higher than 91% throughout the experiment. The systematic uncertainty in the measured asymmetry due to the DAQ deadtime was below 0.2%, and the statistical quality of the asymmetry measurement agreed with a Gaussian distribution to over five orders of magnitude. The systematic uncertainties from the pion contamination and the counting deadtime were therefore both negligible compared to the (3~4)% statistical uncertainty and other leading systematic uncertainties such as the beam polarization. Results presented here demonstrate that accurate asymmetry measurements can be performed with even higher event rates or backgrounds using this type of scaler-based DAQ.

Although the implemented asymmetry corrections (beam polarization, PID efficiency, deadtime, Q^2 , pion dilution, etc.) are the major ones affecting the measured asymmetry, several additional corrections need to be implemented in order to fully extract the final asymmetry. These corrections include:

- electromagnetic radiative corrections for both the internal and the external radiative effects
- contamination of the charged pion asymmetry in the electron trigger
- uncertainty caused by contamination from the target end-caps
- uncertainty from the transverse asymmetry
- background of neutral pions decaying into e^+e^- pairs.

After obtaining the final corrected asymmetry, the quark axial charge ($2C_{2u} - C_{2d}$) can be extracted. Several theoretical works need to be done in order to compare the experimental measured quantity to theoretical predictions. These include:

- hadronic higher-twist effects for interaction between quarks inside the nucleon at low Q^2
- charge symmetry violation between u and d quarks in the proton and neutron
- contribution from higher order Feynman diagrams in addition to the tree-level contribution.

Eventually, our result at $Q^2 = 1.1$ (GeV/c) 2 will set an upper limit on the Q^2 -dependence of the hadronic correction. Assuming the Standard Model value for C_{1q} and no corrections from hadronic effects, we will extract the value of $2C_{2u} - C_{2d}$ from the $Q^2=1.9$ (GeV/c) 2 asymmetry results. The current statistical uncertainty of the asymmetry indicates that we will improve this coupling combination by a factor of five to six compared to the current PDG value [18]. We expect to finalize the analysis and publish these results shortly within a year.

Bibliography

- [1] Y. Qiang, Ph.D. thesis, MIT (2007).
- [2] R. Silwal, Ph.D. thesis, University of Viginia (2012).
- [3] J. Alcorn *et al.*, Nucl. Instrum. Meth. A **522**, 294 (2004).
- [4] M. J. Ramsey-Musolf, Phys. Rev. C **60**, 015501 (1999), arXiv:hep-ph/9903264 .
- [5] A. Czarnecki and W. J. Marciano, arXiv: hep-ph/0003049 .
- [6] P. C. Rowson, D. Su, and S. Willocq, Ann. Rev. Nucl. Part. Sci. **51**, 345 (2001).
- [7] *A Combination of Preliminary Electroweak Measurements and Constraints on the Standard Model.*, Tech. Rep. (CERN-EP/2001-98, 2001) arXiv:hep-ex/0112021 .
- [8] M. Chanowitz, Phys. Rev. Lett. **87**, 231802 (2001).
- [9] K. Kumar *et al.*, SLAC Proposal E-158 .
- [10] P. L. Anthony *et al.* (SLAC E158 Collaboration), Phys. Rev. Lett. **95**, 081601 (2005).
- [11] C. S. Wood *et al.*, Science **275**, 1759 (1997).
- [12] S. C. Bennet and C. E. Wieman, Phys. Rev. Lett. **82**, 2484 (1999).
- [13] A. I. Milstein, O. P. Sushkov, and I. S. Terekhov, Phys. Rev. Lett. **89**, 283003 (2002).

- [14] G. P. Zeller *et al.* (The NuTeV Collaboration), Phys. Rev. Lett. **88**, 091802 (2002).
- [15] J. T. Londergan and A. W. Thomas, Phys. Lett. B **558**, 132 (2003).
- [16] D. S. Armstrong *et al.*, Qweak Proposal, JLab E02-020, arXiv:1202.1255v2 .
- [17] X. Zheng *et al.*, PVDIS Proposal, JLab E08-011, hallaweb.jlab.org/experiment/PVDIS/ref/PR_pvdis2.pdf.
- [18] Particle Data Group, <http://pdg.lbl.gov>, Phys. Rev. D **66**, 010001 (2002).
- [19] C. Y. Prescott *et al.*, Phys. Lett. B **77**, 347 (1978).
- [20] R. N. Cahn and F. J. Gilman, Phys. Rev. D **17**, 1313 (1978).
- [21] S. Eidelman *et al.*, Phys. Lett. B **592**, 1 (2004).
- [22] P. Bosted *et al.* (SLAC E149 collaboration), DIS-Parity: Parity violation in deep-inelastic electron scattering, SLAC Proposal E-149 (1993).
- [23] C. Sinclair *et al.*, Phys. Rev. ST Accel. Beams **10**, 023501 (2007).
- [24] J. Hansknecht *et al.*, Phys. Rev. ST Accel. Beams **13**, 010101 (2010).
- [25] E. Chudakov, O. Glamazdin, *et al.*, “The moller polarimeter,” <http://hallaweb.jlab.org/equipment/beam/beampol/beampolar.html>.
- [26] M. Baylac, E. Burtin, C. Cavata, S. Escoffier, B. Frois, D. Lhuillier, F. Marie, J. Martino, *et al.*, Phys. Lett. B **539**, 8 (2002).
- [27] D. Neyret, T. Pussieux, T. Auger, M. Baylac, E. Burtin, C. Chipaux, S. Escoffier, *et al.*, Nucl. Instrum. Meth. A **443**, 231 (2000).
- [28] M. Friend, D. parno, F. Benmokhar, A. Camsonne, M. Dalton, G. B. Franklin, V. Mamyan, R. Michaels, *et al.*, Nucl. Instrum. Meth. A **676**, 96 (2012).
- [29] K. A. Aniol *et al.* (HAPPEX Collaboration), Phys. Lett. B **509**, 211 (2001).

- [30] K. A. Aniol *et al.* (HAPPEX Collaboration), Phys. Rev. C **69**, 065501 (2004).
- [31] K. A. Aniol *et al.* (HAPPEX Collaboration), Phys. Rev. Lett. **635**, 275 (2006).
- [32] A. Acha *et al.* (HAPPEX Collaboration), Phys. Rev. Lett. **98**, 032301 (2007).
- [33] Z. Ahmed *et al.* (HAPPEX Collaboration), Phys. Rev. Lett. **108**, 102001 (2012).
- [34] S. Abrahamyan *et al.*, Phys. Rev. Lett. **108**, 112502 (2012).
- [35] C. Horowitz *et al.*, Phys. Rev. C **85**, 032501(R) (2012).
- [36] K. D. Paschke, Eur. Phys. J. A **32**, 549 (2007).
- [37] *Helicity Clock Generator*, Tech. Rep. (JLAB-TN-01-035).
- [38] W. Barry, Nucl. Instr. Methods **301**, 407 (1991).
- [39] K. Unser, IEEE Trans. Nucl. Sci. **NS-28**, 2344 (1981).
- [40] X. Zheng, Ph.D. thesis, MIT (2002).
- [41] R. S. Holmes, “The parity analyzer (pan),” <http://www.phy.syr.edu/~rsholmes/happex/pan/html/index.html>.
- [42] N. Liyanage, Spectrometer constant determination for the Hall A HRS pair, JLab-TN-01-049, 2001 .